JVI Accepted Manuscript Posted Online 23 March 2016
J. Virol. doi:10.1128/JVI.03259-15

MUTAGENESIS OF CORONAVIRUS NSP14 REVEALS ITS POTENTIAL ROLE IN MODULATION OF THE INNATE IMMUNE RESPONSE

Martina Becares, Alejandro Pascual-Iglesias, Aitor Nogales*, Isabel Sola, Luis Enjuanes# and Sonia Zuñiga

Department of Molecular and Cell Biology. National Center of Biotechnology (CNB-CSIC), Campus Universidad Autónoma de Madrid. Darwin 3. Madrid, Spain.

* Present address: Department of Microbiology and Immunology, University of Rochester, Rochester, New York, USA.

Running Head: Modulation of antiviral response by coronavirus nsp14

Corresponding author
Luis Enjuanes
Department of Molecular and Cell Biology
Centro Nacional de Biotecnología, CNB-CSIC
Darwin, 3
Campus Universidad Autónoma de Madrid
28049 Madrid, Spain
Phone 34-91- 585 4555
E-mail: L.Enjuanes@cnb.csic.es

Abstract word count: 233 Manuscript text word count: 6902

ABSTRACT

Coronavirus (CoV) non-structural protein 14 (nsp14) is a 60 kDa protein encoded by the replicase gene that is part of the replication-transcription complex. It is a bifunctional enzyme bearing 3'-5' exoribonuclease (ExoN) and guanine-N7-methyltransferase (N7-MTase) activities. ExoN hydrolyzes single- and double-stranded RNAs and is part of a proofreading system responsible for the high fidelity of CoV replication. Nsp14 N7-MTase activity is required for viral mRNA cap synthesis and prevents the recognition of viral mRNAs as "non-self" by the host cell. In this work, a set of point mutants affecting different motifs within the ExoN domain of nsp14 was generated, using transmissible gastroenteritis virus as a model of *Alphacoronavirus*. Mutants lacking ExoN activity were non-viable despite being competent in both viral RNA and protein synthesis. A specific mutation within zinc finger 1 (ZF-C) led to a viable virus with growth and viral RNA synthesis kinetics similar to that of the parental virus. Mutant rTGEV-ZF-C caused decreased cytopathic effect and apoptosis compared with the wild-type virus and reduced levels of dsRNA accumulation at late times post-infection. Consequently, the mutant triggered a reduced antiviral response, which was confirmed by evaluating different stages of the dsRNA-induced antiviral pathway. The expression of IFN-β, TNF, and interferon-stimulated genes in cells infected with mutant rTGEV-ZF-C was reduced, when compared to the parental virus. Overall, our data revealed a potential role for CoV nsp14 in modulation of the innate immune response.

IMPORTANCE

The innate immune response is the first line of antiviral defense that culminates in the synthesis of interferon and proinflammatory cytokines to control viral replication. CoVs have evolved several mechanisms to counteract the innate immune response at different

levels, but to date the role of CoV-encoded ribonucleases in preventing activation of the dsRNA-induced antiviral response has not been described. The introduction of a mutation in zinc finger 1 of the ExoN domain of nsp14 led to a virus that induced a weak antiviral response, most likely due to the accumulation of lower levels of dsRNA in the late phases of infection. These observations allowed us to propose a novel role for CoV nsp14 ExoN activity in counteracting the antiviral response, which could serve as a novel target for the design of antiviral strategies.

INTRODUCTION

Coronaviruses (CoVs) are enveloped, single-stranded, positive-sense RNA viruses belonging to the *Coronaviridae* family within the *Nidovirales* order (1). CoVs are frequently associated with respiratory and enteric diseases in humans, livestock, and companion animals (2, 3). CoVs have been divided into four genera: *Alphacoronavirus*, such as human coronavirus 229E (HCoV-229E) or the porcine transmissible gastroenteritis virus (TGEV); *Betacoronavirus,* that includes the severe acute respiratory syndrome coronavirus (SARS-CoV) and the recently emerged Middle East respiratory syndrome CoV (MERS-CoV), both causing pneumonia and having a high mortality rate; *Gammacoronavirus*, including infectious bronchitis virus (IBV); and *Deltacoronavirus* (4). CoVs contain the largest known genome among RNA viruses, consisting of a single-stranded, positive-sense, 5′-capped and polyadenylated RNA molecule of 27-31 kb in length (5). The first two-thirds of the genome contains the replicase gene, which is comprised of two overlapping open reading frames (ORFs), 1a and 1b. After infection, viral genomic RNA (gRNA) is directly translated to yield two polyprotein precursors, pp1a and pp1ab, the latter requiring ribosomal frameshifting near the 3′ end of ORF1a for its translation (6). Subsequently, the two polyproteins are cleaved by ORF1a-encoded proteases to release a total of 16 nonstructural proteins (nsp1 to nsp16) (7, 8). These nsps assemble together with cellular factors to form a large replication-transcription complex (RTC) associated with membrane structures derived from the endoplasmic reticulum (9-11). The RTC is required for CoV RNA synthesis, which is comprised of genome replication and transcription. CoV transcription is a discontinuous process that yields a nested set of subgenomic mRNAs (sg mRNAs) that serve as templates for translation of the viral structural and accessory proteins (8, 12, 13). The CoV RTC is extremely complex, and apart from the RNA-dependent RNA

Journal of Virology

82 polymerase (RdRp) and helicase activities common to many RNA viruses, CoVs
83 encode a unique set of RNA-modifying activities such as the 3′-5′ exoribonuclease
84 (ExoN) and the uridylate-specific endoribonuclease (NendoU), a recently discovered
85 nucleotidyltransferase (14), or enzymatic activities related to the synthesis of the cap
86 structure, such as RNA 5′-triphosphatase (RTPase), N7-methyltransferase (N7-MTase),
87 and 2′-O methyltransferase (2O-MTase) (7, 15, 16).
88 CoV nsp14 is a bifunctional enzyme that harbors both ExoN and N7-MTase activities
89 (17-19). The amino-terminal part of nsp14 includes the ExoN active core, which is
90 divided into three motifs: I (DE), II (E) and III (D). Due to this characteristic, CoV
91 nsp14 is included in the DEDD exonuclease superfamily, which comprises cellular
92 enzymes that catalyze DNA proofreading (20). Nsp14 ExoN has been proposed to have
93 a critical role in CoV replication and transcription, as mutants lacking this activity
94 showed an important reduction in viral RNA synthesis or accumulation (17, 21). Nsp14
95 hydrolyzes single- and double- stranded RNA (ssRNA and dsRNA) to final products of
96 8-12 nt and 5-7 nt, respectively, and its nucleolytic activity is enhanced up to 35 fold by
97 interaction with nsp10 (17, 22). In addition, nsp14 ExoN activity was proposed to be
98 part of the RNA proofreading machinery during CoV replication (20, 23), which would
99 be required for the replication and maintenance of the large CoV genome. In fact, only
100 larger-sized Nidovirus genomes encode ExoN activity (24). Mutations in the ExoN
101 active core abolishing the exonuclease activity led to CoVs that exhibited a 15-20 fold
102 increase in replication errors in *Betacoronavirus* such as MHV and SARS-CoV (21, 23,
103 25). As a proofreading component, ExoN should be involved in the removal of
104 misincorporated nucleotides. Indeed, nsp14 activity efficiently removed mismatched 3′-
105 end nucleotides mimicking RdRp misincorporation products (22). Moreover, mutants
106 lacking ExoN activity showed greater sensitivity to the mutagen 5-fluorouracil, in

contrast to CoVs with ExoN activity, which are considered resistant to lethal mutagenesis (26).

The carboxy-terminal part of nsp14 contains N7-MTase activity, involved in the addition of a methyl group to the cap guanosine at the N7 position, leading to formation of the cap-0 structure (18, 27). In general, this cap-0 is critical for efficient export, translation, and stability of mRNAs. In addition, the methylation of N7 would be required for the subsequent methylation at the O-2′ position, which is essential for prevention of viral RNA recognition by the host immune system (28-30).

The bifunctional nsp14 is part of the large multi-subunit polymerase complex described as the core of the CoV RTC, which integrates RNA polymerization, proofreading, and cap-modifying activities into a multifunctional protein assembly (16, 31).

The recent crystallization of the SARS-CoV nsp14 identified the presence of three zinc fingers (ZFs) within the nsp14 structure (32). A ZF is a small, independently folded domain that is structured around a zinc ion, which is coordinated through cysteine and histidine residues. ZFs are structurally diverse, with more than 40 types of annotated ZFs in UniProtKB, and are found in proteins that perform a broad range of functions, including essential cellular processes such as replication, signaling, cell proliferation, or apoptosis (33). ZFs usually function as interaction modules and bind to a wide variety of compounds, such as nucleic acids, proteins, and small molecules (34). While interaction of different ZF types with DNA has been well characterized in terms of affinity and specificity, ZF interactions with RNA remains poorly characterized (35). Nevertheless it has been shown that modification of a ZF sequence may alter its binding to an RNA substrate (36).

Viral dsRNA produced as a replication intermediate is a pathogen-associated molecular pattern (PAMP), which mediates the activation of well characterized antiviral

mechanisms leading to shutdown of protein synthesis, stimulation of host innate immunity for initial detection of pathogens, and subsequent activation of adaptive immunity (37, 38). CoVs have evolved mechanisms impairing the activation of the innate immune response at different stages. These mechanisms include the production of several viral proteins that interfere with type I interferon (IFN) and proinflammatory cytokine production (39) and the induction of double-membrane vesicles, where dsRNA is shielded from innate immune sensing by cytoplasmic receptors (10).

As a key enzyme in cap formation, CoV nsp14 was proposed as an IFN antagonist (39). In fact, overexpression studies have revealed that nsp14 acts as an IFN antagonist (40), although it has not been determined whether this activity is linked to its ExoN or N7-MTase domains. The second CoV-encoded ribonuclease, NendoU, is also a robust IFN antagonist when overexpressed (41). The possibility that CoV ribonucleases could degrade dsRNA PAMPs has been suggested as an additional mechanism preventing IFN induction during CoV infection (42). Nevertheless, the role of these proteins in preventing the innate immune response has not been studied so far.

Current knowledge about CoV nsp14 is mainly derived from study of the Betacoronaviruses. In contrast, there is limited information on the role of *Alphacoronavirus* nsp14 during infection, as HCoV-229E mutations which abrogated ExoN activity were lethal (17). In this work we used another *Alphacoronavirus*, TGEV, to analyze the role of the nsp14 ExoN domain in terms of virus viability and induction of antiviral response. Our results show that mutations abolishing ExoN activity resulted in only a modest decrease in viral RNA synthesis, but recovery of infectious progeny failed, something that may be a general characteristic for alphacoronaviruses. A specific mutation in the ZF1 produced a viable virus causing a decrease in accumulation of dsRNA intermediates at late times post-infection. Consequently, this mutant virus

triggered a reduced antiviral response and apoptosis in comparison to the parental virus, indicating that CoV nsp14 plays a role in modulation of the innate immune response.

MATERIALS AND METHODS

Cells. Baby hamster kidney cells (BHK-21) (ATCC CCL-10), or BHK-21 cells stably transformed with the gene coding for porcine aminopeptidase N (BHK-pAPN) (43) were grown in Dulbecco's modified Eagle's medium (DMEM) supplemented with 5% fetal calf serum (FCS). Both cell lines were transfected with the Sindbis virus replicon pSINrep1 (44) expressing TGEV nucleocapsid (N) protein, obtaining BHK-N or BHK-pAPN-N cells, respectively. G418 (1.5 mg/ml) and puromycin (5 μg/ml) were used as selection agents for pAPN and pSINrep1, respectively. Recombinant TGEV viruses obtained in this work were grown in swine testis (ST) cells (45) using DMEM supplemented with 10% FCS.

Plasmid constructs. cDNAs of TGEV-derived replicons and infectious viruses (46, 47) were generated by PCR-directed mutagenesis. To generate nsp14-ExoI, nsp14-ExoIII, nsp14-ZF-H, nsp14-ZF-C and nsp14-N7MTase mutant sequences, two overlapping PCR fragments were obtained by using as a template the plasmid pBAC-TGEV (47), containing the full-length TGEV genome (GeneBank accesion number AJ271965). The 5′ fragment was obtained by using the forward primer nsp13-finVS (5′-CATGTGTGATAGAACTATGTATGAGAATCTTG-3′) and the specific reverse primer shown in Table 1. The 3′ fragment was obtained by using the specific forward primer shown in Table 1 and, in all cases, the reverse primer nsp15prin-RS (5′-CCATTATTTTGTCAGCAATAACAGCAG-3′). Full-length amplicons were generated by overlap extension of 3′ and 5′ PCR products using primers nsp13-finVS and

nsp15prin-RS. In all cases, full-length amplicons were digested with BstBI and XbaI restriction enzymes and cloned into the same sites of plasmid pSL-nsp14, which includes the TGEV genomic sequence from nt 15,063-21,504, leading to intermediate plasmids pSL-nsp14-ExoI, pSL-nsp14-ExoIII, pSL-nsp14-ZF-H, pSL-nsp14-ZF-C and pSL-nsp14-N7MTase. All intermediate plasmids were digested with NheI and PacI restriction enzymes and inserts were cloned into the same sites of pBAC-REP2 (46), generating the mutant replicons pBAC-REP2-nsp14-ExoI, pBAC-REP2-nsp14-ExoIII, pBAC-REP2-nsp14-ZF-H, pBAC-REP2-nsp14-ZF-C, and pBAC-REP2-nsp14-N7MTase. Alternatively, inserts digested with NheI and PacI restriction enzymes were cloned into the same sites of plasmid pBAC-TGEV-$S_{7.1}$ (C.M. Sanchez, M. Becares, S. Zuñiga, and L. Enjuanes, unpublished results) leading to pBAC-TGEV-$S_{7.1}$-nsp14-ExoI, pBAC-TGEV-$S_{7.1}$-nsp14-ExoIII, pBAC-TGEV-$S_{7.1}$-nsp14-ZF-H, pBAC-TGEV-$S_{7.1}$-nsp14-ZF-C, and pBAC-TGEV-$S_{7.1}$-nsp14-N7MTase. All cloning steps were checked by sequencing of the PCR fragments and cloning junctions. For each mutant sequence, two independent cDNAs were constructed.

Production of a polyclonal antibody specific for TGEV nsp14. An nsp14 protein with a 6-His tag fused at its N-terminus was expressed in the baculovirus-insect cell system, using a baculovirus obtained from the Fei Deng laboratory (Wuhan Institute of Virology, Wuhan, China). Recombinant nsp14 was purified to near homogeneity by metal chelate affinity chromatography using Ni-NTA agarose (Sigma-Aldrich, Madrid, Spain) following standard procedures set up in our laboratory (48). Specific polyclonal antisera were generated by Biogenes GmbH (Germany) after immunization of rabbits with purified recombinant nsp14.

Transfection and recovery of infectious rTGEVs from cDNA clones. BHK-pAPN-N or BHK-N cells grown to 90% confluence in 35 mm plates (or 12-well plates for RNA synthesis experiments) were transfected using 3.3 µg of the corresponding pBAC and 10 µl of Lipofectamine 2000 (Invitrogen) per million cells according to the manufacturer's specifications. For recovery of infectious recombinant TGEVs (rTGEVs) from cDNA infectious clones, BHK-pAPN-N transfected cells were trypsinized at 6 h post-trasfection (hpt) and plated over confluent ST monolayers grown in 35 mm plates. After a 2-day incubation period, the cell supernatants were harvested (passage 0) (49).

Viral RNA presence at passages 0 and 1 was analyzed by RT-PCR. Total cellular RNA was extracted using the RNeasy Mini kit (Qiagen) following the manufacturer's instructions. DNA was removed by treatment of 7 µg of each purified RNA with 20 U of DNase I (Roche) for 30 min at 37 °C, and DNA-free RNAs were re-purified using the RNeasy Mini kit (Qiagen). Reverse transcription was performed with the High Capacity RNA-to-cDNA™ Kit (Life Technologies) according to the manufacturer's instructions. PCRs were performed to analyze genomic RNA (gRNA) by amplifying nsp14 sequences (using the forward primer nsp13fin_VS and the reverse primer nsp15prin_RS), and mRNA of the N protein using the forward primer SP (5′-GTGAGTGTAGCGTGGCTATATCTCTTC-3′) and the reverse primer N-479RS (5′-TAGATTGAGAGCGTGACCTTG-3′).

Each rTGEV was cloned by three plaque purification steps and the resultant virus was grown and titrated as previously described (50). Lysis plaque diameter was determined by measuring the area of the lysis plaques using the software ImageJ (51).

Full genome sequencing of each rTGEV clone was performed using overlapping PCRs covering the entire TGEV genome (primer sequences available on request). Both

strands of each PCR product were sequenced, and contigs were assembled using SeqMan software from DNASTAR Lasergene® package (SeqMan®. Version 8.0.2 DNASTAR. Madison, WI).

Analysis of viral RNA synthesis and cellular gene expression by quantitative RT-PCR (RT-qPCR). Total intracellular RNA was extracted at 24 hpt from transfected BHK-N cells, or at the indicated times post-infection from ST cells infected with rTGEVs. Total RNA was purified with the RNeasy Mini kit (Qiagen) according to the manufacturer's specifications. For the analysis of viral RNA synthesis in transfected cells, an additional step was used in order to remove DNA from samples. For this purpose, 7 µg of each RNA was treated with 20 U of DNase I (Roche) for 30 min at 37 °C. DNA-free RNA was re-purified using the RNeasy Mini kit (Qiagen). In all cases, 100 ng of total RNA was used as the template for synthesis of cDNA with random hexamers using the High-capacity cDNA transcription kit (Life Technologies) following the manufacturer's instructions.

Viral RNA levels were evaluated by RT-qPCR using custom TaqMan assays (Life Technologies) specific for the TGEV genomic RNA (gRNA) and subgenomic mRNA 7 (mRNA-7), both in positive (+) and negative (-) polarity (Table 2), following standard procedures set up in our laboratory (52). Cellular gene expression was analyzed using TaqMan gene expression assays (Applied Biosystems) specific for porcine genes encoding TNF (Ss03391318_g1), IFN-β (Ss03378485_u1), IRF-1 (Ss03388785_m1), MDA5 (Ss03386373_u1), RIG-I (Ss03381552_u1), or TFG-β (Ss03382325_u1), and porcine 2′,5′ oligoadenylate synthetase 1 (OAS1) was analyzed by using a custom TaqMan gene expression assay (53). The β-glucuronidase (GUSB) gene (TaqMan code Ss03387751_u1) was used as a reference housekeeping gene, since its expression

remains constant in both infected and non-infected cells (54). Data were acquired with a 7500 real-time PCR system (Applied Biosystems) and analyzed with 7500 software v2.0.6. The relative quantifications were performed using the $2^{-\Delta\Delta Ct}$ method (55). All experiments and data analyses were MIQE compliant (56).

Protein analysis by Western blot. Transfected BHK-N cells and infected ST cells were collected at the indicated times, and cell lysates were obtained by solubilizing cells in 1x SDS gel-loading sample buffer (57). Cell lysates were resolved by denaturing electrophoresis in NuPAGE 4-12% Bis-Tris gels with 3-morpholinopropane-1-sulfonic acid (MOPS) SDS running buffer (Invitrogen) and transferred to polyvinylidene difluoride (PVDF) membranes (*Immobilon®-P PVDF*, Merk-Millipore) employing a Trans-Blot® Turbo™ Transfer System (Bio-Rad), using the manufacturer's recommended conditions. Membranes were blocked for 1 h at room temperature (RT) with 5% skim milk in TBS (20 mM Tris-HCl pH 7.5, 150 mM NaCl) and then incubated with monoclonal antibodies (mAbs) specific for TGEV N protein (mAb-3DC10) (58), or β-Actin (Abcam, 1:10,000). Polyclonal antibodies (pAb) against active caspase 3 protein (Abcam, 1:1000), or TGEV nsp3 (59) were also used. The blots were then incubated with a horseradish peroxidase-conjugated secondary antibody diluted in TBS supplemented with 0.1% Tween 20 (TTBS) and 3% skim milk for 1 h at RT. After extensive washing with TTBS, the immune complexes were detected using Clarity™ Western ECL Blotting Substrate (Bio-Rad) and the ChemiDoc XRS^{+} System (Bio-Rad), according to the manufacturer's instructions.

Protein amounts were estimated by densitometric analysis using ImageLab 4.1 software (BioRad). At least three different experiments and appropriate gel exposures were used

in all cases with similar results. In addition, different exposures of the same experiment were analyzed to assure that data were obtained from films within the linear range.

Immunofluorescence analysis. ST cells were grown on 12 mm glass coverslips in DMEM 10% FCS to a confluence of 30–50%, and then cell cultures were synchronized by serum deprivation (60). Briefly, cells were rinsed with phosphate-buffered saline (PBS) and incubated with DMEM 0.1% FCS for 48 h, as it had been previously determined that this incubation time allows for 85-90% of ST cells in G0 phase. After serum starvation, cells were released into cell cycle by incubation in DMEM-10% FCS for 4 h and subsequently mock-infected or infected at a multiplicity of infection (moi) of 2 with each rTGEV. At 8 or 16 hpi, cells were washed with PBS, fixed with 4% paraformaldehyde, permeabilized with cold methanol for 10 min and blocked in PBS with 10% FCS for 45 min at RT. mAb specific for dsRNA (SCICONS English & Scientific Consulting Kft, 1:200) and pAb specific for TGEV nsp14 (1:1000, see above) were used. Bound primary antibodies were detected with Alexa Fluor 488- or 594-conjugated antibodies specific for mouse or rabbit IgG, respectively (1:500, Invitrogen). Cell nuclei were stained with 4′, 6-diamidino-2-phenylindole (DAPI) (1:200, Sigma). Confocal microscopy was performed using a Leica SP5 laser scanning microscope, and images were collected and processed with LAS AF software (Leica, Wetzlar, Germany). Quantification of the intensity of the fluorescence was done by measuring the mean grey fluorescence of individual cells from grey-scale projections of microscopy images. The variance of the intensity was also determined and the normalized optical density variance was calculated as an indicator of signal dispersion, as previously described (61). Data represents the average of 30 individual cell measurements.

Polyinosinic:polycytidylic acid [poly(I:C)] treatment. ST cells were grown to confluence in 24-well plates and infected with rTGEVs at an moi of 1. At 12 hpi, infected cells were transfected with 0.5 µg of poly(I:C) (Sigma-Aldrich) per well using Lipofectamine 2000 (Invitrogen), according to the manufacturer's instructions. At 4 hpt, total intracellular RNA was extracted and analyzed by RT-qPCR, as described above. Total cell RNA integrity was evaluated with a Bioanalyzer 2100 (Agilent Technologies) following the manufacturer's recommendations, and analyzed with 2100 Expert software (Agilent Technologies).

Statistical analysis. Two-tailed, unpaired Student's *t*-tests were used to analyze the difference in mean values between groups. All results were expressed as mean ± standard deviation; *P* values <0.05 were considered significant.

RESULTS

Analysis of RNA synthesis by nsp14-ExoN mutants. CoV nsp14 has been proposed to play a role in RNA synthesis, although the specific mechanism has not been determined (17, 20). In addition, there is limited information on the role of *Alphacoronavirus* ExoN in the infection context. Therefore, a set of four TGEV ExoN domain mutants was engineered by reverse genetics using a TGEV-derived replicon (46). Nsp14 is highly conserved among different CoV genera, and all the previously described motifs were identified in TGEV nsp14 (Fig. 1A). Two of the mutants were designed to affect the catalytic residues DE/D within the conserved exonuclease motifs ExoI and Exo III, respectively (Fig. 1A). These mutations are well characterized *in vitro* as abolishing ExoN activity in the case of HCoV-229E and SARS-CoV (17, 18). The

recent publication of the SARS-CoV nsp14 protein crystal structure has revealed the presence of two ZFs in the ExoN domain of the protein, which seem essential for the function of nsp14 (Fig. 1A) (32). Two mutants affecting ZF1 were engineered, designed to alter the ZF type but theoretically still allowing zinc coordination. The ZF2 motif was not modified as it overlaps with the catalytic core, and its modification would most likely influence nsp14 catalytic activity. An additional TGEV mutant replicon modifying the N7-MTase domain was designed as a control, as it was previously shown that this mutation has no effect on ExoN activity (32). The mutant replicons were transfected into BHK-N cells (52), and replication and transcription levels were analyzed at 24 hpt by RT-qPCRs measuring the accumulation of gRNA and mRNA-7, respectively. RNA levels were compared in all cases with those obtained from a non-replicative replicon, which served to establish background reference levels of replication and transcription due to the cytomegalovirus promoter. As expected, the engineered mutation in the N7-MTase domain did not have any impact on RNA synthesis (Fig. 1B). The ExoI and ExoIII mutations led to a modest reduction of approximately 3 fold that was barely statistically significant in both replication and transcription when compared to the WT replicon, indicating that these mutants were competent in RNA synthesis (Fig. 1B). Interestingly, the engineered mutations in ZF1 led to two different outcomes. Mutant ZF-H showed a modest reduction in replication in comparison to WT levels, while the level of mRNA-7 was comparable to that of the non-replicative replicon, indicating that the ZF-H mutation completely abolished transcription (Fig. 1B). In contrast, the ZF-C mutant was competent in both replication and transcription (Fig. 1B).

Journal of Virology

Mutations abolishing ExoN activity resulted in a lethal phenotype. To study the role of TGEV ExoN activity during infection, the ExoI and ExoIII mutant infectious viral cDNAs were generated. The mutant cDNAs were transfected into BHK-pAPN cells expressing TGEV N protein that were plated over ST cells, susceptible to viral infection. At 48 hpt, cell supernatants were harvested (passage 0) and used to infect ST cells (passage 1), following the standard protocol set up in the laboratory (49). No cytopathic effect was observed after ExoI or ExoIII mutant cDNA transfection (data not shown). In order to analyze whether viral RNA synthesis occurred, total RNA was extracted from passage 0 and passage 1 and the presence of viral RNA was evaluated by RT-PCR. Viral genomic RNA (gRNA) corresponding to nsp14 sequences, as well as the mRNA of N protein (mRNA-N) produced by WT virus were detected both at passage 0 and 1, indicating an efficient virus recovery (Fig. 2A). In contrast, gRNA and mRNA-N synthesized from rTGEV ExoN mutants were only amplified from passage 0 samples and not detected at passage 1, indicating a failure in mutant virus recovery (Fig. 2A). Sequencing of the nsp14 gRNA fragment confirmed that each rTGEV carried the desired engineered mutations.

In order to determine whether a defect in RNA synthesis prevented recovery of mutant viruses, RNA accumulation was analyzed by RT-qPCR 24 hours after transfection of the ExoN mutant cDNAs into BHK-N cells. Results indicated a decrease in replication (15 fold reduction) and transcription (2 fold reduction, not statistically significant), compared to WT cDNAs (Fig. 2B). A similar reduction in the accumulation of viral RNA was observed both for the positive and negative strands (Fig. 2B). These data are in agreement with the decrease in viral RNA synthesis observed for HCoV-229E, MHV, and SARS-CoV (17, 21). Nevertheless, in the case of MHV and SARS-CoV, this reduction in viral RNA synthesis did not prevent virus recovery. Moreover, previous

Journal of Virology

rTGEV mutants obtained in our laboratory that had a higher reduction in RNA synthesis led to the recovery of viable viruses (62), suggesting that there is another cause for the lethal phenotype of TGEV ExoI and ExoIII mutants.

As nsp14 has also a role in cap synthesis, mutations could have an effect on viral protein accumulation, although it has been demonstrated that SARS-CoV ExoI and ExoIII mutants were competent in N7-MTase activity (19). Variation in protein synthesis of the rTGEV mutants was evaluated by Western blot. Accumulation of nsp3, which is directly translated from gRNA, did not vary significantly with respect to WT virus despite the reduction of gRNA levels (Fig. 2C), suggesting that viral protein synthesis was not affected in the ExoI and ExoIII mutants. Unfortunately, detection of other viral structural proteins after cDNA transfection failed even for WT virus, due to low BAC transfection efficiency.

Altogether, the results indicate that ExoN activity is required for TGEV viability. Similar results were obtained with HCoV229E (17), therefore the requirement of ExoN activity may be common to all members of the *Alphacoronavirus* genus.

Effect of mutations in nsp14 zinc finger 1 in viral phenotype. In order to study the functional role of nsp14 ZF1 in the context of CoV infection, rTGEV infectious clones harboring the ZF-H and ZF-C mutations were engineered. As expected, the ZF-H virus was not recovered (data not shown), probably due to similar viral RNA transcription defects as those observed with the replicon system (Fig. 1B). Interestingly, MHV substituting two Zn coordinating residues by alanine also led to a lethal phenotype (63), suggesting an important role for ZF1 in nsp14 function.

The rTGEV-ZF-C virus was successfully recovered with a titer of 4.3×10^7 pfu/ml, similar to that of the WT virus (8.7×10^7 pfu/ml). The introduced mutations were present

405 in the recovered mutant virus, even after 10 passages in cell cultures of plaque-purified
406 viruses, indicating that they were stably maintained in the rTGEV genome. Moreover,
407 the full-length genomes of two independent clones of rTGEV-WT and rTGEV-ZF-C
408 were sequenced, and the only differences found between the rTGEV-WT and the
409 rTGEV-ZF-C were the desired engineered mutations.
410 Infection with rTGEV-ZF-C induced a delayed cytopathic effect (CPE) in comparison
411 to rTGEV-WT, and lysis plaques formed by rTGEV-ZF-C were significantly smaller
412 (half size of diameter) than those from rTGEV-WT (Fig. 3A). This plaque size
413 reduction was observed both when analyzing uncloned viruses obtained from
414 transfection and in plaques formed by six individual clones (data not shown). Viral
415 growth was analyzed at different times post-infection, at both low (0.05) and high (5)
416 moi. Infectious titer of rTGEV-ZF-C was up to 10 fold higher than that of rTGEV-WT
417 at early times post-infection, although maximum titer observed from 24 hpi was
418 identical to that of the rTGEV-WT (Fig. 3B).
419 Both rTGEV-ZF-C and rTGEV-WT showed the same gRNA accumulation kinetics at
420 early times post-infection, corresponding with the active RNA synthesis stage of the
421 TGEV infectious cycle (Fig. 3C), in agreement with our observations using TGEV
422 replicons (Fig. 1B). Nevertheless, at late times post-infection, rTGEV-ZF-C
423 accumulated lower levels of gRNA than rTGEV-WT (Fig. 3C). This data, together with
424 the reduced CPE and smaller plaque phenotype, could be attributed to a less efficient
425 dissemination of the rTGEV-ZF-C in comparison to rTGEV-WT.
426
427 **Antiviral response elicited by rTGEV-ZF-C.** Previous results from our laboratory
428 indicated that CPE produced by TGEV and lysis plaque size could correlate with
429 apoptosis induction as a consequence of the host antiviral response (53). TGEV induces

apoptosis following a caspase-dependent pathway that involves the processing of two initiator proteases (caspase 8 and 9), as well as three downstream effector caspases (caspases 3, 6 and 7) (64, 65). To evaluate whether rTGEV-ZF-C CPE and lysis plaque size reduction were due to reduced apoptosis, caspase 3 activation was evaluated by Western blot using specific antibodies. At 24 hpi, when rTGEV-ZF-C and rTGEV-WT infectious titers were similar (Fig. 3B), rTGEV-ZF-C was found to induce lower levels of active caspase 3 in comparison to the rTGEV-WT (Fig. 4A and B, left pannels). It has been described that TGEV N protein is cleaved by caspases within the host cell (66). In agreement with the reduced caspase 3 activation, decreased cleavage of N protein by caspases was observed during rTGEV-ZF-C infection in comparison to rTGEV-WT (Fig. 4A and B, right pannels). Altogether, these results indicated that the rTGEV-ZF-C virus triggered a reduced apoptosis.

TGEV-induced apoptosis is linked to the antiviral response produced during infection (53, 54). Therefore, accumulation of IFN-β and TNF mRNAs was measured as a marker of the activation of the IRF-3 and NFκβ pathways, respectively, during the dsRNA-triggered antiviral response. rTGEV-ZF-C infection led to significantly reduced levels of IFN-β (up to 25 fold) and TNF (up to 17 fold) in comparison to rTGEV-WT infection (Fig. 5A). The induction of interferon-stimulated genes (ISGs) was also evaluated, by measuring the accumulation of IRF-1, OAS, RIG-I, and MDA-5 mRNAs. In agreement with the reduced IFN-ß production, a significant decrease in the expression of these genes was observed in rTGEV-ZF-C when compared to rTGEV-WT-infected cells (Fig. 5B). In contrast, the accumulation of TGFβ mRNA, whose expression did not change with TGEV infection (54), was similar in both cases (Fig. 5B), discarding a general decrease of host cell transcription after rTGEV-ZF-C infection.

454 Overall, these results indicated that rTGEV-ZF-C triggered a reduced antiviral response
455 in comparison to that induced by rTGEV-WT.
456
457 **dsRNA accumulation in rTGEV-ZF-C infected cells.** In non-immune cells, RIG-I
458 and MDA-5 cytoplasmic sensors mainly mediate the production of cytokines and IFN.
459 These proteins recognize the presence of dsRNAs in the cytoplasm, activating
460 transcription factors IRF-3 and NF-κB, which finally leads to the expression of type I
461 IFN and proinflammatory cytokines, respectively (67). Because rTGEV-ZF-C infection
462 led to reduced IFN-β and TNF accumulation, dsRNA levels were analyzed by
463 immunofluorescence in synchronized and infected ST cells. Nsp14 was also detected by
464 immunofluorescence to analyze the effect of ZF1 mutation on nsp14 protein subcellular
465 location. The nsp14-ZF-C mutant protein localized similarly to the WT protein (Fig.
466 6A), with a pattern similar to that of other viral proteins present in the CoV RTC such
467 as nsp3 (data not shown) (59).
468 At early times post-infection, no differences in dsRNA distribution pattern were
469 observed in rTGEV-ZF-C and rTGEV-WT infected cells (Fig. 6A, 8 hpi panels). Co-
470 localization between nsp14 and dsRNA was observed, probably corresponding to active
471 sites of viral RNA synthesis (Fig. 6A, lower 8 hpi panels). At late times post-infection,
472 dsRNA labeling produced a scattered pattern in rTGEV-WT infected cells, uniformly
473 distributed throughout the cytoplasm (Fig. 6A, middle 16 hpi panels). This dsRNA
474 pattern was previously observed in CoV infection at late hpi, (10, 68). In contrast,
475 dsRNA was still concentrated in well-defined perinuclear granules in rTGEV-ZF-C
476 infected cells (Fig. 6A, 16 hpi panels). In order to quantify the cytoplasmic dsRNA
477 accumulation and distribution, the mean intensity of fluorescence as well as the
478 normalized variance of the intensity of fluorescence were measured in thirty individual

cells. In the case of a uniform distribution of the signal the variance is minimal, while its value increases when the signal is irregularly distributed (61). An un-biased analysis showed that, at early times post-infection, no significant differences were observed in both mean and variance of intensity between rTGEV-ZF-C and rTGEV-WT infected cells (Fig. 6B). In contrast, significant reduction in the intensity of fluorescence was observed in rTGEV-ZF-C infected cells compared to the rTGEV-WT (Fig 6B). Moreover, the quantification of the signal distribution resulted in a significant increase in the normalized variance in the case of rTGEV-ZF-C infected cells, which meant a reduction in the spreading of the signal in comparison to that of the rTGEV-WT infected cells (Fig 6B). This result suggested that the nsp14-ZF-C mutation interfered with dsRNA accumulation at late times post-infection, which may be the cause for the reduced induction of subsequent antiviral responses.

Modulation of innate immune response by nsp14-ZF-C. To further investigate whether rTGEV-ZF-C actively inhibits the cytoplasmic accumulation of dsRNA and, as a consequence, the activation of the subsequent antiviral response, the dsRNA-sensing pathway was activated by the addition of exogenous dsRNA in the context of viral infection.

In order to evaluate the potential of rTGEV-WT or rTGEV-ZF-C viruses in the inhibition of dsRNA-triggered antiviral responses, ST cells were infected with rTGEV-ZF-C or rTGEV-WT at an moi of 1 and at 12 hpi transfected with the dsRNA analog poly(I:C). At 4 hpt, viral RNA accumulation and the induction of the innate immune response were analyzed by measuring gRNA, IFN-β, and TNF mRNA accumulation by RT-qPCR. In the absence of poly(I:C), IFN-β and TNF mRNA production were significantly reduced in rTGEV-ZF-C infected cells, as described above (Fig. 7A).

Poly(I:C) treatment did not significantly affect virus production, as similar gRNA levels were detected in the absence and presence of poly(I:C) (Fig. 7A). rTGEV-WT virus together with poly(I:C) triggered an exacerbated innate immune response, as expected from the combined action of rTGEV-WT infection and the dsRNA analog poly(I:C) (Fig. 7A). In contrast, this response was significantly reduced in the case of rTGEV-ZF-C infection, despite the exogenous activation by poly(I:C) (Fig. 7A).

To test whether during rTGEV-ZF-C mutant virus infection the decreased dsRNA levels led to a reduced recognition and, subsequently to a diminished innate immune response, RNase L activation was analyzed. As previously described, rTGEV-WT infection hardly produces RNase L activation and RNA degradation (53). In agreement with this data, no significant difference in RNA degradation was observed for the rTGEV-ZF-C mutant infected cells compared with those infected with the parental virus (Fig. 7B). In contrast, when RNase L activation was triggered by exogenous dsRNA [poly(I:C)] transfection together with infection, a significant decrease was observed in RNA degradation during rTGEV-ZF-C infection compared with rTGEV-WT infection (Fig. 7B). These results indicated that indeed during rTGEV-ZF-C infection there was a decreased dsRNA recognition, as expected due to the lower dsRNA accumulation, which, in consequence, caused a reduced IFN production.

In a complementary approach, co-infections with rTGEV-ZF-C and rTGEV-WT were performed in order to evaluate whether the antiviral response elicited by rTGEV-WT infection was modulated by the rTGEV-ZF-C virus. ST cells were infected at different moi of each virus, and IFN-β and TNF mRNA accumulation were evaluated by RT-qPCR at 16 hpi. A slight difference in gRNA levels between rTGEV-ZF-C and rTGEV-WT, which as shown above does not influence infectious titers, was also observed during independent infections (Fig. 8). No significant differences in gRNA

accumulation were detected during co-infections (Fig. 8). Moreover, the nsp14 region was sequenced and the proportion of each rTGEV at the moment of the analysis was estimated to be similar to the one in the inoculum (data not shown). A decreased innate immune response was observed in cells co-infected with rTGEV-ZF-C and rTGEV-WT at a 1:1 ratio, and more significantly in co-infections at a 5:1 ratio, when compared to the same dose of rTGEV-WT alone (Fig. 8). This result suggests that the nsp14-ZF-C mutation could be acting *in trans*, reducing the dsRNA produced during rTGEV-WT infection and, as a consequence, decreasing the subsequent innate immune response. Furthermore, this data strongly suggests that the mutant virus actively reduced the antiviral response triggered by the parental virus, as IFNß and TNF accumulation were not the sum of those induced by each virus independently and, in fact, the reduction was dependent on the moi used for the rTGEV-ZF-C virus.

Altogether these data indicate that rTGEV-ZF-C leads to a reduction in accumulation of dsRNA, either exogenous or that produced during infection. Our results indicate that CoV nsp14 modulates the innate immune response most likely by affecting dsRNA accumulation.

DISCUSSION

Previous studies have shown that CoV ExoN activity is required for the high-fidelity replication of CoV genome (21, 25). Although there is extensive knowledge on *Betacoronavirus* ExoN functions during infection, the function of *Alphacoronavirus* ExoN during infection has not been analyzed apart from biochemical characterization *in vitro*. In this study, we generated a set of mutants in different domains of TGEV ExoN, based on the published structure of nps14 (32). Mutants with abrogated ExoN activity were lethal, despite being competent in viral RNA and protein synthesis. The reduction

554 in viral RNA synthesis reported here for TGEV and previously for HCoV229E (17) was
555 similar to that observed for the analogous equivalent viable mutants in *Betacoronavirus*,
556 such as SARS-CoV (21). Therefore, the reduction in RNA synthesis is most likely not
557 itself the causative factor for the lethality of the ExoN mutations.
558 Mutagenesis of a residue in the ZF1 motif, included in the ExoN domain of nsp14, led
559 to viable viruses reaching an infectious titer similar to that of the parental virus. The
560 rTGEV-ZF-C mutant accumulated lower amounts of dsRNA in the cytoplasm, and
561 subsequently triggered a reduced antiviral response, as evidenced by decreased levels of
562 IFN-β and TNF mRNAs. This work showed for the first time that CoV ExoN domain,
563 beyond its well-known role in proofreading, participates in innate immune response
564 modulation.
565 The relevance of nsp14 ZF1 motif was previously suggested by biochemical studies
566 (32), as well as reverse genetics analyses, which led to non-recovery of a virus carrying
567 mutations to alanine of the ZF1 domain residues responsible for zinc coordination (63).
568 Structural data, together with the fact that those mutations severely altering the ZF were
569 lethal in MHV, whereas MHV mutants lacking ExoN activity were viable (21, 63),
570 strongly suggest that this domain is not directly involved in ExoN catalytic activity.
571 Although the ZF1 motif may have a role in the maintenance of specific interactions of
572 the nsp14 protein with its RNA substrate or other RTC proteins. Our data support the
573 relevance of this domain, as conservative mutations theoretically allowing zinc
574 coordination, such as the ZF-H mutant, completely abolished transcription in both
575 replicon and virus systems. In addition, our data were also in agreement with ZF1 motif
576 not being directly involved in ExoN catalytic activity, as preliminary sequencing data
577 has shown similar mutation rates between rTGEV-WT and rTGEV-ZF-C viruses (data
578 not shown).

579 As other ZF motifs, the ExoN ZF1 domain may have a role in RNA-nsp14 interaction,
580 and therefore mutations in ZF1 may impact its properties in terms of affinity and/or
581 specificity. *In vitro* studies have revealed that CoV nsp14 binds to both ssRNA and
582 dsRNA with no sequence specificity, although data indicated that ExoN activity is much
583 higher in substrates with dsRNA structure (22). ZFs are typically involved in protein
584 binding to nucleic acids (35), though unfortunately the recent nsp14 crystallographic
585 structure does not include an RNA substrate, so the specific RNA-protein interactions
586 involving each ZF motif were not elucidated (32). The molecular bases for the
587 mechanism by which ZF proteins recognize dsRNA are complex, as they are highly
588 dependent on contact with phosphates and hydrophobic interactions (69). This
589 complexity makes it difficult to predict how mutations may impact the binding
590 properties of a ZF-containing protein to its substrate. Further analyses on the nsp14 ZF-
591 C mutant protein exonuclease or N7-MTase activities, or RNA binding ability, are
592 required to decipher the role of nsp14 in the dsRNA response modulation. This would
593 require in vitro analysis with the purified WT and ZF-C nsp14 proteins (17, 28).
594 Moreover, to determine the role on ExoN activity purified nsp10 should also be
595 included (22). This would represent an extensive biochemical characterization that
596 would be the aim of future work.
597 In spite of reaching similar infectious titer and gRNA accumulation, cells infected with
598 mutant rTGEV-ZF-C accumulated lower levels of dsRNA than the rTGEV-WT infected
599 cells. Two alternative explanations are compatible with this fact: (i) the ZF-C mutant
600 degrades dsRNA more efficiently than the WT virus, or (ii) the ZF-C mutant generates
601 lower amounts of dsRNA intermediates during infection. Nevertheless, the biochemical
602 activity of nsp14 as an RNase, which has been clearly reported *in vitro* (17, 22), is
603 hardly compatible with a role in generating dsRNA. Moreover, the fact that rTGEV-ZF-

C reduced the antiviral response triggered both by exogenous dsRNA [poly(I:C)] or infection-produced dsRNA (during co-infections of WT and mutant viruses) makes the first hypothesis more feasible. Therefore, our data suggests that nsp14 ExoN plays a role in degrading dsRNA intermediates that could act as PAMPs, triggering the subsequent immune response. In this working model (Fig. 9), the engineered rTGEV-ZF-C mutant was more efficient in this task, leading to reduced amounts of dsRNA and, subsequently, inducing a very weak innate immune response.

Theoretically, it would be expected that a reduced antiviral response should lead to an increase in viral replication, eventually leading to higher virus titers. On the other hand, as viruses evolve leading to optimum replication in a cell host, it is quite frequent that, in cell cultures any disturbance in host antiviral response does not cause a significant effect in virus titers. This seems to be the case for TGEV virus infecting porcine ST cells, as mutant viruses causing increased antiviral response replicate to similar titers as wild-type virus in tissue cultures (53). In line with that observation, the decreased IFN production caused by the rTGEV-ZF-C mutant virus did not lead to an increased viral titer. It is worth noting that rTGEV-WT infection of ST cells produce around 35 pg/ml of IFNß (54). This concentration is much lower than that required to affect TGEV replication. In fact, we have found that a concentration of 9000 pg/ml of IFNß is required to cause a 20-fold decrease in viral titer (M. Becares, S. Zuñiga and L. Enjuanes, unpublished data). Therefore, it was not surprising that in our experimental conditions, it was not possible to detect an effect on virus titers of the ZF-C mutation.

To our knowledge, this work represents the first link of CoV ExoN activity and the degradation of dsRNA leading to innate immune suppression, although this function of CoV nsp14 ExoN was recently hypothesized (42). Beyond CoVs, only arenaviruses encode a protein with exonuclease activity within their genome. Similar to CoV nsp14,

629 the arenavirus nucleoprotein (NP) has cap binding function and carries 3′-5′
630 exonuclease activity, degrading short RNA molecules and inhibiting IFN production in
631 arenavirus infected cells. Studies revealed that mutants lacking the 3′-5′ exonuclease
632 activity do not inhibit IFN induction, strongly implicating it in modulation of cellular
633 antiviral responses (70-72). Additionally, it has been shown that the arenavirus NP
634 directly interacts with the cytosolic RNA sensors RIG-I and MDA-5 (73), giving
635 support to the hypothesis that degradation of dsRNA PAMPs by the arenavirus
636 exonuclease avoids further recognition by RIG-I or MDA5. In the case of CoVs, which
637 efficiently inhibit IFN induction during infection, nsp14 could also be acting by
638 degrading dsRNA PAMPs. Interestingly, CoV nsp14 is known to interact with the
639 cellular helicase DDX1, which has recently been described as a cytosolic dsRNA sensor
640 that activates type I IFN responses (74).
641 In agreement with our working model hypothesis (Fig. 9), CoV mutants lacking ExoN
642 activity would trigger an exacerbated innate immune response. An enhanced antiviral
643 response, together with the reported defects in viral RNA synthesis and the increased
644 mutation rate, could contribute to the lethal phenotype observed for *Alphacoronaviruses*
645 lacking ExoN activity. In fact, SARS-CoV ExoN mutants were rescued in Vero cells,
646 defective in IFN synthesis, and MHV ExoN mutants rescue was initially impaired when
647 IFN competent cells were used (63, and M. Denison, personal communication). SARS-
648 CoV lacking ExoN activity are attenuated in young and aged diseased mice, showing a
649 faster clearance than the WT virus (75). This phenotype could be compatible with the
650 triggering of a higher innate immune response by these mutants, although this aspect
651 was not analyzed.
652 Further studies are needed to understand the role of ribonucleases, both ExoN and
653 NendoU, in antagonizing the activation of the dsRNA-induced antiviral response in the

654 different CoV genera. These proteins may counteract the innate immune response by
655 degrading dsRNA and limiting activation of antiviral pathways by cytosolic sensors,
656 and therefore they may serve as targets for the design of novel antiviral strategies.
657
658 **ACKNOWLEDGEMENTS**
659 We thank Marga González and Carlos Sánchez for their technical assistance.
660 This work was supported by grants from the Government of Spain (BIO2013-42869-R),
661 a U.S. National Institutes of Health (NIH) project (2P01AI060699-06A1), and financial
662 support of IMI and European Commission and in-kind contributions from EFPIA
663 partners (ZAPI project, IMI Grant Agreement nº115760). MB and SZ received a
664 contract from Government of Spain and NIH.
665
666 **REFERENCES**
667 1. **de Groot RJ, Baker SC, Baric R, Enjuanes L, Gorbalenya AE, Holmes KV,**
668 **Perlman S, Poon L, Rottier PJM, Talbot PJ, Woo PCY, Ziebuhr J.** 2012.
669 Coronaviridae, p. 774-796. *In* King AMQ, Adams MJ, Carstens EB, Lefkowitz
670 EJ (ed.), Virus Taxonomy: Ninth Report of the International Committee on
671 Taxonomy of Viruses. Elsevier Academic Press, San Diego.
672 2. **Masters PS.** 2006. The molecular biology of coronaviruses. Adv. Virus Res.
673 **66:**193-292.
674 3. **Perlman S, Netland J.** 2009. Coronaviruses post-SARS: update on replication
675 and pathogenesis. Nat. Rev. Microbiol. **7:**439-450.
676 4. **de Groot RJ, Baker SC, Baric RS, Brown CS, Drosten C, Enjuanes L,**
677 **Fouchier RA, Galiano M, Gorbalenya AE, Memish ZA, Perlman S, Poon**
678 **LL, Snijder EJ, Stephens GM, Woo PC, Zaki AM, Zambon M, Ziebuhr J.**

679 2013. Middle East respiratory syndrome coronavirus (MERS-CoV):
680 announcement of the Coronavirus Study Group. J. Virol. **87:**7790-7792.
681 5. **Enjuanes L, Gorbalenya AE, de Groot RJ, Cowley JA, Ziebuhr J, Snijder**
682 **EJ.** 2008. The Nidovirales, p. 419-430. *In* Mahy BWJ, Van Regenmortel M,
683 Walker P, Majumder-Russell D (ed.), Encyclopedia of Virology, Third Edition.
684 Elsevier Ltd., Oxford.
685 6. **Brierley I, Digard P, Inglis SC.** 1989. Characterization of an efficient
686 coronavirus ribosomal frameshifting signal: requirement for an RNA
687 pseudoknot. Cell **57:**537-547.
688 7. **Ziebuhr J.** 2005. The coronavirus replicase, p. 57-94. *In* Enjuanes L (ed.),
689 Coronavirus replication and reverse genetics, vol. 287. Springer-Verlag, Berlin-
690 Heidelberg.
691 8. **Sola I, Almazán F, Zúñiga S, Enjuanes L.** 2015. Continuous and
692 discontinuous RNA synthesis in coronaviruses. Annu. Rev. Virol. **2**.
693 9. **van Hemert MJ, van den Worm SH, Knoops K, Mommaas AM,**
694 **Gorbalenya AE, Snijder EJ.** 2008. SARS-coronavirus replication/transcription
695 complexes are membrane-protected and need a host factor for activity in vitro.
696 PLoS pathogens **4:**e1000054.
697 10. **Knoops K, Kikkert M, Worm SH, Zevenhoven-Dobbe JC, van der Meer Y,**
698 **Koster AJ, Mommaas AM, Snijder EJ.** 2008. SARS-coronavirus replication is
699 supported by a reticulovesicular network of modified endoplasmic reticulum.
700 PLoS Biol. **6:**e226.
701 11. **Gosert R, Kanjanahaluethai A, Egger D, Bienz K, Baker SC.** 2002. RNA
702 replication of mouse hepatitis virus takes place at double-membrane vesicles. J.
703 Virol. **76:**3697-3708.

704 12. **Enjuanes L, Almazan F, Sola I, Zuñiga S, Alvarez E, Reguera J, Capiscol**
705 **C.** 2006. Biochemical aspects of coronavirus replication. Adv. Exp. Med. Biol.
706 **581:**13-24.
707 13. **Sawicki SG, Sawicki DL, Siddell SG.** 2007. A contemporary view of
708 coronavirus transcription. J. Virol. **81:**20-29.
709 14. **Lehmann KC, Gulyaeva A, Zevenhoven-Dobbe JC, Janssen GM, Ruben M,**
710 **Overkleeft HS, van Veelen PA, Samborskiy DV, Kravchenko AA,**
711 **Leontovich AM, Sidorov IA, Snijder EJ, Posthuma CC, Gorbalenya AE.**
712 2015. Discovery of an essential nucleotidylating activity associated with a newly
713 delineated conserved domain in the RNA polymerase-containing protein of all
714 nidoviruses. Nucleic Acids Res.**:**DOI:10.1093/nar/gkv1838.
715 15. **Gorbalenya AE, Enjuanes L, Ziebuhr J, Snijder EJ.** 2006. Nidovirales:
716 evolving the largest RNA virus genome. Virus Res. **117:**17-37.
717 16. **Sevajol M, Subissi L, Decroly E, Canard B, Imbert I.** 2014. Insights into
718 RNA synthesis, capping, and proofreading mechanisms of SARS-coronavirus.
719 Virus Res. **194:**90-99.
720 17. **Minskaia E, Hertzig T, Gorbalenya AE, Campanacci V, Cambillau C,**
721 **Canard B, Ziebuhr J.** 2006. Discovery of an RNA virus 3'->5' exoribonuclease
722 that is critically involved in coronavirus RNA synthesis. Proc. Natl. Acad. Sci.
723 USA **103:**5108-5113.
724 18. **Chen Y, Cai H, Pan J, Xiang N, Tien P, Ahola T, Guo D.** 2009. Functional
725 screen reveals SARS coronavirus nonstructural protein nsp14 as a novel cap N7
726 methyltransferase. Proc. Natl. Acad. Sci. USA **106:**3484-3489.

19. **Chen Y, Tao J, Sun Y, Wu A, Su C, Gao G, Cai H, Qiu S, Wu Y, Ahola T, Guo D.** 2013. Structure-function analysis of severe acute respiratory syndrome coronavirus RNA cap guanine-N7-methyltransferase. J. Virol. **87:**6296-6305.

20. **Denison MR, Graham RL, Donaldson EF, Eckerle LD, Baric RS.** 2011. Coronaviruses: an RNA proofreading machine regulates replication fidelity and diversity. RNA Biol. **8:**270-279.

21. **Eckerle LD, Lu X, Sperry SM, Choi L, Denison MR.** 2007. High fidelity of murine hepatitis virus replication is decreased in nsp14 exoribonuclease mutants. J. Virol. **81:**12135-12144.

22. **Bouvet M, Imbert I, Subissi L, Gluais L, Canard B, Decroly E.** 2012. RNA 3'-end mismatch excision by the severe acute respiratory syndrome coronavirus nonstructural protein nsp10/nsp14 exoribonuclease complex. Proc. Natl. Acad. Sci. USA **109:**9372-9377.

23. **Smith EC, Sexton NR, Denison MR.** 2014. Thinking outside the triangle: Replication fidelity of the largest RNA viruses. Ann. Rev. Virol. **1:**111-132.

24. **Smith EC, Denison MR.** 2012. Implications of altered replication fidelity on the evolution and pathogenesis of coronaviruses. Curr. Opin. Virol. **2:**519-524.

25. **Eckerle LD, Becker MM, Halpin RA, Li K, Venter E, Lu X, Scherbakova S, Graham RL, Baric RS, Stockwell TB, Spiro DJ, Denison MR.** 2010. Infidelity of SARS-CoV nsp14-exonuclease mutant virus replication is revealed by complete genome sequencing. PLoS pathogens **6:**e1000896.

26. **Smith EC, Blanc H, Vignuzzi M, Denison MR.** 2013. Coronaviruses lacking exoribonuclease activity are susceptible to lethal mutagenesis: evidence for proofreading and potential therapeutics. PLoS pathogens **9:**e1003565.

751 27. **Decroly E, Ferron F, Lescar J, Canard B.** 2012. Conventional and
752 unconventional mechanisms for capping viral mRNA. Nat. Rev. Microbiol.
753 **10:**51-65.
754 28. **Bouvet M, Debarnot C, Imbert I, Selisko B, Snijder EJ, Canard B, Decroly**
755 **E.** 2010. In vitro reconstitution of SARS-coronavirus mRNA cap methylation.
756 PLoS pathogens **6:**e1000863.
757 29. **Zust R, Cervantes-Barragan L, Habjan M, Maier R, Neuman BW, Ziebuhr**
758 **J, Szretter KJ, Baker SC, Barchet W, Diamond MS, Siddell SG, Ludewig B,**
759 **Thiel V.** 2011. Ribose 2'-O-methylation provides a molecular signature for the
760 distinction of self and non-self mRNA dependent on the RNA sensor Mda5. Nat.
761 Immunol. **12:**137-143.
762 30. **Daffis S, Szretter KJ, Schriewer J, Li J, Youn S, Errett J, Lin TY, Schneller**
763 **S, Zust R, Dong H, Thiel V, Sen GC, Fensterl V, Klimstra WB, Pierson TC,**
764 **Buller RM, Gale M, Jr., Shi PY, Diamond MS.** 2010. 2'-O methylation of the
765 viral mRNA cap evades host restriction by IFIT family members. Nature
766 **468:**452-456.
767 31. **Smith EC, Denison MR.** 2013. Coronaviruses as DNA wannabes: a new model
768 for the regulation of RNA virus replication fidelity. PLoS pathogens
769 **9:**e1003760.
770 32. **Ma Y, Wu L, Shaw N, Gao Y, Wang J, Sun Y, Lou Z, Yan L, Zhang R, Rao**
771 **Z.** 2015. Structural basis and functional analysis of the SARS coronavirus
772 nsp14-nsp10 complex. Proc. Natl. Acad. Sci. USA **112:**9436-9441.
773 33. **Laity JH, Lee BM, Wright PE.** 2001. Zinc finger proteins: new insights into
774 structural and functional diversity. Curr. Opin. Struct. Biol. **11:**39-46.

775 34. **Krishna SS, Majumdar I, Grishin NV.** 2003. Structural classification of zinc
776 fingers: survey and summary. Nucleic Acids Res. **31:**532-550.
777 35. **Iuchi S, Kuldell N.** 2005. Zinc Finger Proteins: From Atomic Contact to
778 Cellular Function, 1st. ed. Landes Bioscience, and Kluwer Academic,Plenum
779 Publishers, New York, USA.
780 36. **Friesen WJ, Darby MK.** 1998. Specific RNA binding proteins constructed
781 from zinc fingers. Nat. Struct. Biol. **5:**543-546.
782 37. **Medzhitov R, Janeway CA, Jr.** 1997. Innate immunity: the virtues of a
783 nonclonal system of recognition. Cell **91:**295-298.
784 38. **Kawai T, Akira S.** 2006. Innate immune recognition of viral infection. Nat.
785 Immunol. **7:**131-137.
786 39. **Totura AL, Baric RS.** 2012. SARS coronavirus pathogenesis: host innate
787 immune responses and viral antagonism of interferon. Curr. Opin. Virol. **2:**264-
788 275.
789 40. **Zhang Q, Shi K, Yoo D.** 2016. Suppression of type I interferon production by
790 porcine epidemic diarrhea virus and degradation of CREB-binding protein by
791 nsp1. Virology **489**:252-268.
792 41. **Frieman M, Ratia K, Johnston RE, Mesecar AD, Baric RS.** 2009. Severe
793 acute respiratory syndrome coronavirus papain-like protease ubiquitin-like
794 domain and catalytic domain regulate antagonism of IRF3 and NF-kappaB
795 signaling. J. Virol. **83:**6689-6705.
796 42. **Kindler E, Thiel V.** 2014. To sense or not to sense viral RNA-essentials of
797 coronavirus innate immune evasion. Curr. Opin. Microbiol. **20C:**69-75.
798 43. **Delmas B, Gelfi J, Kut E, Sjostrom H, Noren O, Laude H.** 1994.
799 Determinants essential for the transmissible gastroenteritis virus-receptor

interaction reside within a domain of aminopeptidase-N that is distinct from the enzymatic site. J. Virol. **68:**5216-5224.

44. **Frolov I, Hoffman TA, Prágai BM, Dryga SA, Huang HV, Schlesinger S, Rice CM.** 1996. Alphavirus-based expression vectors: Strategies and applications. Proc. Natl. Acad. Sci. USA **93:**11371-11377.

45. **McClurkin AW, Norman JO.** 1966. Studies on transmissible gastroenteritis of swine. II. Selected characteristics of a cytopathogenic virus common to five isolates from transmissible gastroenteritis. Can. J. Comp. Med. Vet. Sci. **30:**190-198.

46. **Almazan F, Galan C, Enjuanes L.** 2004. The nucleoprotein is required for efficient coronavirus genome replication. J. Virol. **78:**12683-12688.

47. **Almazan F, Gonzalez JM, Penzes Z, Izeta A, Calvo E, Plana-Duran J, Enjuanes L.** 2000. Engineering the largest RNA virus genome as an infectious bacterial artificial chromosome. Proc. Natl. Acad. Sci. USA **97:**5516-5521.

48. **Nogales A, Galan C, Marquez-Jurado S, Garcia-Gallo M, Kremer L, Enjuanes L, Almazan F.** 2011. Immunogenic characterization and epitope mapping of transmissible gastroenteritis virus RNA dependent RNA polymerase. J. Virol. Methods **175:**7-13.

49. **Almazan F, Galan C, Enjuanes L.** 2008. Engineering infectious cDNAs of coronavirus as bacterial artificial chromosomes. Methods in molecular biology **454:**275-291.

50. **Jimenez G, Correa I, Melgosa MP, Bullido MJ, Enjuanes L.** 1986. Critical epitopes in transmissible gastroenteritis virus neutralization. J. Virol. **60:**131-139.

824 51. **Abramoff MD, Magalhães PJ, Ram SJ.** 2004. Image processing with ImageJ.
825 Biophotonics international **11:**36-42.
826 52. **Zuñiga S, Cruz JL, Sola I, Mateos-Gomez PA, Palacio L, Enjuanes L.** 2010.
827 Coronavirus nucleocapsid protein facilitates template switching and is required
828 for efficient transcription. J. Virol. **84:**2169-2175.
829 53. **Cruz JLG, Sola I, Becares M, Alberca B, Plana J, Enjuanes L, Zuñiga S.**
830 2011. Coronavirus gene 7 counteracts host defenses and modulates virus
831 virulence. PLoS pathogens **7:**e1002090.
832 54. **Cruz JLG, Becares M, Sola I, Oliveros JC, Enjuanes L, Zuñiga S.** 2013.
833 Alphacoronavirus protein 7 modulates host innate immune response. J. Virol.
834 **87:**9754-9767.
835 55. **Livak KJ, Schmittgen TD.** 2001. Analysis of relative gene expression data
836 using real-time quantitative PCR and the 2(-Delta Delta C(T)) Method. Methods
837 **25:**402-408.
838 56. **Bustin SA, Benes V, Garson JA, Hellemans J, Huggett J, Kubista M,**
839 **Mueller R, Nolan T, Pfaffl MW, Shipley GL, Vandesompele J, Wittwer CT.**
840 2009. The MIQE guidelines: minimum information for publication of
841 quantitative real-time PCR experiments. Clin. Chem. **55:**611-622.
842 57. **Sambrook J, Russell DW.** 2001. Molecular cloning: A laboratory manual, 3rd
843 ed. Cold Spring Harbor Laboratory Press, Cold Spring Harbor, New York.
844 58. **Martín-Alonso JM, Balbín M, Garwes DJ, Enjuanes L, Gascón S, Parra F.**
845 1992. Antigenic structure of transmissible gastroenteritis virus nucleoprotein.
846 Virology **188:**168 - 174.
847 59. **Nogales A, Marquez-Jurado S, Galan C, Enjuanes L, Almazan F.** 2012.
848 Transmissible gastroenteritis coronavirus RNA-dependent RNA polymerase and

nonstructural proteins 2, 3, and 8 are incorporated into viral particles. J. Virol. **86:**1261-1266.

60. **Langan TJ, Chou RC.** 2011. Synchronization of mammalian cell cultures by serum deprivation. Methods in molecular biology **761:**75-83.

61. **Iborra FJ, Buckle V.** 2008. Wide confocal cytometry: a new approach to study proteomic and structural changes in the cell nucleus during the cell cycle. Histochem. Cell Biol. **129:**45-53.

62. **Zuñiga S, Sola I, Alonso S, Enjuanes L.** 2004. Sequence motifs involved in the regulation of discontinuous coronavirus subgenomic RNA synthesis. J. Virol. **78:**980-994.

63. **Eckerle LD, Brockway SM, Sperry SM, Lu X, Denison MR.** 2006. Effects of mutagenesis of murine hepatitis virus nsp1 and nsp14 on replication in culture. Adv. Exp. Med. Biol. **581:**55-60.

64. **Eleouet JF, Chilmonczyk S, Besnardeau L, Laude H.** 1998. Transmissible gastroenteritis coronavirus induces programmed cell death in infected cells through a caspase-dependent pathway. J. Virol. **72:**4918-4924.

65. **Sirinarumitr T, Kluge JP, Paul PS.** 1998. Transmissible gastroenteritis virus induced apoptosis in swine testes cell cultures. Arch. Virol. **143:**2471-2485.

66. **Eleouet JF, Slee EA, Saurini F, Castagné N, Poncet D, Garrido C, Solary E, Martin SJ.** 2000. The viral nucleocapsid protein of transmissible gastroenteritis coronavirus (TGEV) is cleaved by caspase-6 and -7 during TGEV-induced apoptosis. J. Virol. **74:**3975-3983.

67. **Gantier MP, Williams BR.** 2007. The response of mammalian cells to double-stranded RNA. Cytokine Growth Factor Rev. **18:**363-371.

68. **Sola I, Galan C, Mateos-Gomez PA, Palacio L, Zuñiga S, Cruz JL, Almazan F, Enjuanes L.** 2011. The polypyrimidine tract-binding protein affects coronavirus RNA accumulation levels and relocalizes viral RNAs to novel cytoplasmic domains different from replication-transcription sites. J. Virol. **85:**5136-5149.

69. **Brown RS.** 2005. Zinc finger proteins: getting a grip on RNA. Curr. Opin. Struct. Biol. **15:**94-98.

70. **Hastie KM, Kimberlin CR, Zandonatti MA, MacRae IJ, Saphire EO.** 2011. Structure of the Lassa virus nucleoprotein reveals a dsRNA-specific 3' to 5' exonuclease activity essential for immune suppression. Proc. Natl. Acad. Sci. USA **108:**2396-2401.

71. **Qi X, Lan S, Wang W, Schelde LM, Dong H, Wallat GD, Ly H, Liang Y, Dong C.** 2010. Cap binding and immune evasion revealed by Lassa nucleoprotein structure. Nature **468:**779-783.

72. **Jiang X, Huang Q, Wang W, Dong H, Ly H, Liang Y, Dong C.** 2013. Structures of arenaviral nucleoproteins with triphosphate dsRNA reveal a unique mechanism of immune suppression. J. Biol. Chem. **288:**16949-16959.

73. **Zhou S, Cerny AM, Zacharia A, Fitzgerald KA, Kurt-Jones EA, Finberg RW.** 2010. Induction and inhibition of type I interferon responses by distinct components of lymphocytic choriomeningitis virus. J. Virol. **84:**9452-9462.

74. **Zhang Z, Kim T, Bao M, Facchinetti V, Jung SY, Ghaffari AA, Qin J, Cheng G, Liu YJ.** 2011. DDX1, DDX21, and DHX36 helicases form a complex with the adaptor molecule TRIF to sense dsRNA in dendritic cells. Immunity **34:**866-878.

897 75. **Graham RL, Becker MM, Eckerle LD, Bolles M, Denison MR, Baric RS.**
898 2012. A live, impaired-fidelity coronavirus vaccine protects in an aged,
899 immunocompromised mouse model of lethal disease. Nat. Med. **18:**1820-1826.
900

FIGURE LEGENDS

Figure 1. RNA synthesis of TGEV nsp14 mutants. (A) Schematic representation of TGEV nsp14. Exonuclease (ExoN) and N7 methyltransferase (N7-MTase) domains are indicated. Motifs I, II and III conferring the ExoN active site are shown (grey boxes). The three zinc fingers (ZF1, ZF2 and ZF3) are indicated (black boxes), as the amino acids forming the S-adenosylmethionine (SAM) binding pocket in the N7-MTase domain (white box). Within the partial sequence alignments, positions of key amino acids in each motif (white letters in balck boxes) are indicated. Those mutated in each rTGEV construct with respect to the wild-type (WT) sequence are shown as black letters in grey boxes. (B) Quantification of replication and transcription levels in each rTGEV mutant replicon. Non-replicative (NR) and wild-type (WT) replicons were included as controls. Genomic RNA (gRNA) and subgenomic mRNA from gene 7 (mRNA-7) were analyzed by RT-qPCR using specific TaqMan assays after transfection of each replicon in BHK-N cells. Mean values from eight independent transfection experiments are plotted; error bars represent standard deviation. *, p-value < 0.05 **;** **, p-value < 0.01, ***, p-value<0.001.

Figure 2. Analysis of rTGEV ExoN mutants. (A) RT-PCR analysis of viral RNA from passage 0 and passage 1 of rTGEV-ExoI and rTGEV-ExoIII mutants, compared with rTGEV-WT. Genomic (gRNA) and subgenomic mRNA of gene N (mRNA-N) were analyzed. A and B indicate duplicate infectious cDNAs, tested individually for each mutant. Size (bp) of molecular weight markers (Mw) is shown on the right. (B) Quantification of genomic RNA (gRNA) and mRNA of gene 7 (mRNA-7). Both negative and positive strands were measured by RT-qPCR using specific TaqMan assays 24 h post-transfection of infectious cDNAs into BHK-N cells. Means from four

independent transfection experiments are plotted; error bars represent standard deviation. (C) Detection of viral proteins by Western blot. Total protein was extracted 24h after transfection of BHK-N cells with infectious cDNAs from ExoI, ExoIII, WT, a non-replicative rTGEV (NR), or mock transfected cells (M). Viral protein nsp3 and β-actin (as loading control) were detected using specific antibodies. Right panel represents the quantification of the bands by densitometry, corrected by the amount of β-actin. Means from two independent transfection experiments are plotted; error bars represent standard deviation. *, p-value < 0.05 **;** ***, p-value < 0.001.

Figure 3. Growth of nsp14 mutant rTGEV-ZF-C in tissue cultures. (A) Lysis plaques produced by mutant rTGEV-ZF-C and rTGEV-WT at 48 h post-infection in ST cells. Right panel represents the mean diameter of 10 individual lysis plaques; error bars indicate standard deviation. (B) Growth kinetics of rTGEV-WT and rTGEV-ZF-C viruses. ST cells were infected at low (0.05, left) and high (5, right) moi with mutant rTGEV-ZF-C (ZF-C) or rTGEV-WT (WT); supernatants were collected at different times post-infection, and infectious titers were determined by plaque titration on ST cells. Means from three independent experiments are plotted; error bars represent standard deviation. (C) RNA synthesis of rTGEV-WT and rTGEV-ZF-C viruses. ST cells were infected at an moi of 1 with mutant rTGEV-ZF-C or rTGEV-WT; intracellular RNA was collected at different times post-infection, and genomic RNA (gRNA) was quantified by RT-qPCR using specific TaqMan assays. Means from three independent experiments are plotted; error bars represent standard deviation. *, p-value < 0.05 **;** ****,** p-value<0.01; ***, p-value < 0.001.

950 **Figure 4. Induction of apoptosis by mutant rTGEV-ZF-C.** (A) Detection of active
951 caspase 3 (casp3) and TGEV N protein (N) by Western blot. Total protein was extracted
952 from ST cells 24 h after infection with mutant rTGEV-ZF-C, rTGEV-WT, or mock-
953 infected (M). A and B indicate duplicate viral clones that were tested individually.
954 Casp3, N, and β-actin (loading control) were detected using specific antibodies;
955 procaspase 3 (procasp3) and the form of TGEV N protein cleaved by caspases (N-cl)
956 are also indicated. (B) Quantification of the bands by densitometry, corrected by
957 amount of the β-actin. Relative levels of protein (r.u.) were based on comparison with
958 the WT virus, which was considered to be 100%. Means from three independent
959 experiments are plotted; error bars represent standard deviation. *, p-value < 0.05 **; ****,**
960 p-value<0.01.
961
962 **Figure 5. Innate immune response induced by mutant rTGEV-ZF-C.** ST cells were
963 infected with rTGEV-ZF-C or rTGEV-WT virus at an moi of 1, and intracellular RNA
964 was collected at different times post-infection. (A) Quantification of IFN-β and TNF
965 mRNA was performed by RT-qPCR using specific TaqMan assays; relative mRNA
966 levels were based on comparison with mock-infected cells. Means from three
967 independent experiments are plotted; error bars represent standard deviation. (B)
968 Induction of interferon-stimulated genes by rTGEV-ZF-C. Quantification of IRF-1,
969 OAS, RIG-I, MDA5 and TGFß mRNAs was performed by RT-qPCR using specific
970 TaqMan assays; relative mRNA levels were based on comparison with mock-infected
971 cells. Numbers below asterisks indicate the fold change in induction by rTGEV-WT
972 relative to that of mutant rTGEV- ZF-C. Means from four independent experiments are
973 plotted; error bars represent standard deviation. *, p-value < 0.05 **; ****,** p-value<0.01;
974 ***, p-value < 0.001.

975

976 **Figure 6. Accumulation of dsRNA in cells infected with mutant rTGEV-ZF-C.**
977 Confocal microscopy analysis was performed on synchronized ST cells infected with
978 the rTGEV-ZF-C or rTGEV-WT virus at an moi of 1. (A) Immunofluorescence images
979 of ST cells mock-infected (mock) or infected with rTGEV-ZF-C (ZF-C) or rTGEV- WT
980 at 8 and 16 h post-infection. Nsp14 was detected using a specific polyclonal antisera
981 and a secondary antibody staining green; dsRNA was detected using monoclonal
982 antibody mAb-J2 and a secondary antibody staining red; DAPI (4′,6′-diamidino-2-
983 phenylindole) (blue) was used to stain the nuclear DNA. Co-localization is indicated by
984 yellow pixels in the merge panels. (B) Quantification of the mean intensity of
985 fluorescence and normalized standard deviation of fluorescence intensity (intensity
986 variance) of nsp14 and dsRNA. Means of 30 individual cells plotted; error bars
987 represent standard deviation. ***, p-value < 0.001

988

989 **Figure 7. Modulation of dsRNA-induced antiviral response by mutant rTGEV-ZF-**
990 **C.** (A) ST cells were mock-infected (white bars) or infected with mutant rTGEV-ZF-C
991 (grey bars) or rTGEV-WT (black bars) at an moi of 1, and subsequently transfected at
992 12 h post-infection with poly(I:C). At 4 h post-transfection, total intracellular RNA was
993 collected, and quantification of viral genomic RNA (gRNA), IFN-β, and TNF mRNAs
994 was performed by RT-qPCR using specific TaqMan assays. Relative mRNA levels
995 were based on comparison with mock-infected, non-transfected cells. Means from three
996 independent experiments are plotted; error bars represent standard deviation. (B)
997 Cellular RNA integrity. Total RNA was extracted from mock-infected or rTGEV-WT
998 (WT) and rTGEV-ZF-C (ZF) infected ST cells, non-treated (-PolyIC) or treated
999 (+PolyIC) with poly(I:C). The RNA was then analyzed using a Bioanalyzer. The

1000 position of 28S and 18S rRNAs is indicated (left panel). Graph of 28S rRNA integrity,
1001 as measured by the Bioanalyzer. Error bars indicate the standard deviation from four
1002 independent experiments. f.u., fluorescence units. *, p-value < 0.05**;** **, p-value<0.01;
1003 ***, p-value<0.001.
1004
1005 **Figure 8. Modulation of rTGEV-WT induced antiviral response by rTGEV-ZF-C**
1006 **mutant.** ST cells were mock-infected, or individually infected with mutant rTGEV-ZF-
1007 C or rTGEV-WT, or co-infected with each virus at two different ratios (1:1 or 5:1 ZF-
1008 C:WT ratio; the moi of each virus used is indicated by numbers in X-axis). At 16 h
1009 post-infection, total intracellular RNA was collected, and quantification of viral
1010 genomic RNA (gRNA), IFN-β, and TNF mRNAs was performed by RT-qPCR using
1011 specific TaqMan assays. Relative mRNA levels were based on comparison with mock-
1012 infected cells. Means from three independent experiments are plotted; error bars
1013 represent standard deviation. *, p-value < 0.05**;** **, p-value<0.01.
1014
1015 **Figure 9. Working model for the role of nsp14 in the counteraction of antiviral**
1016 **responses during CoV infection.** Schematic overview of the host cell dsRNA-induced
1017 antiviral pathway. The proposed mechanism of action for CoV nsp14 is indicated.
1018

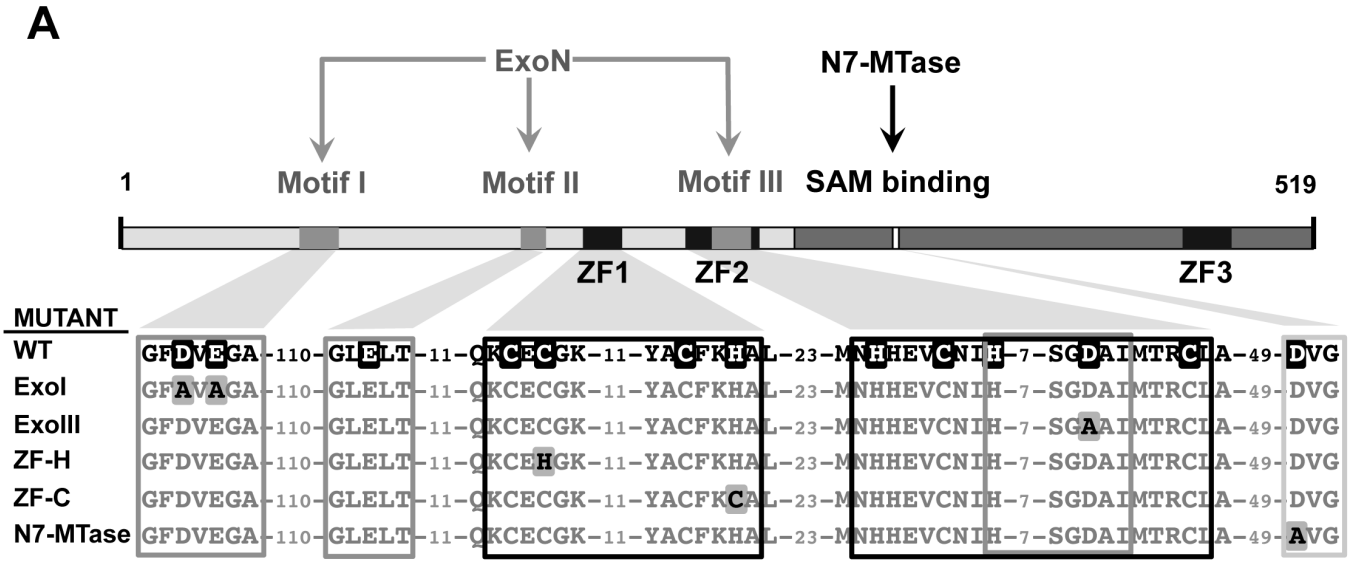

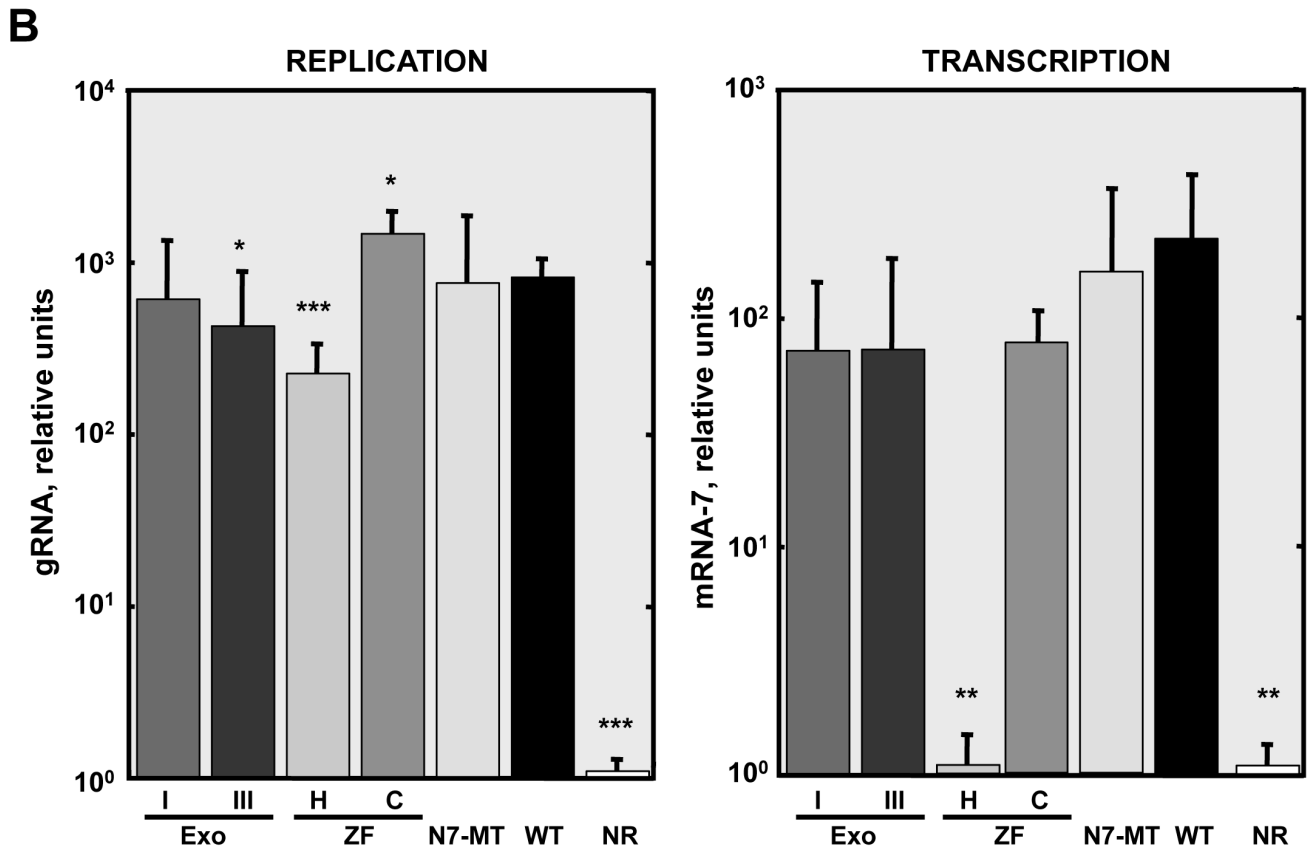

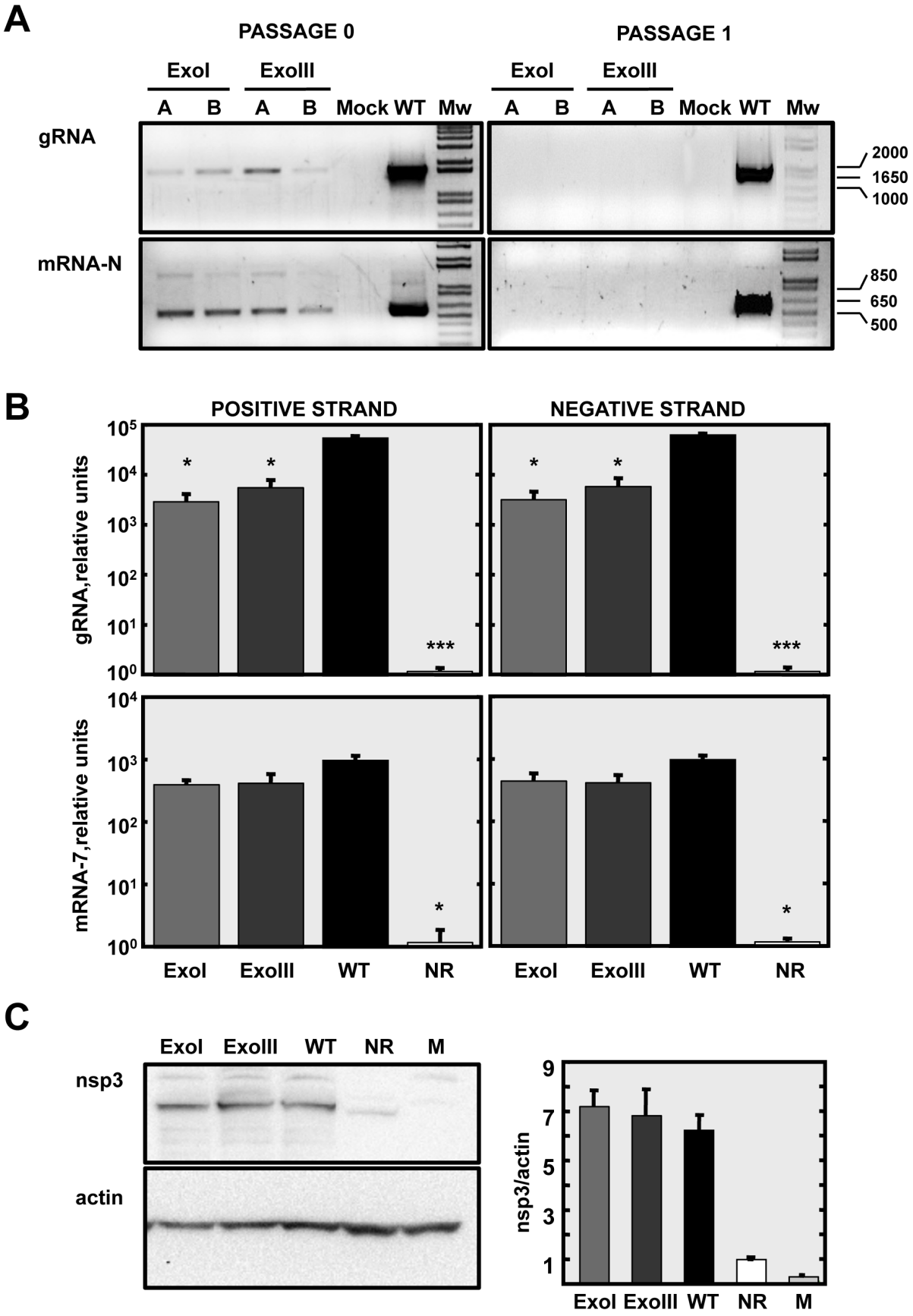

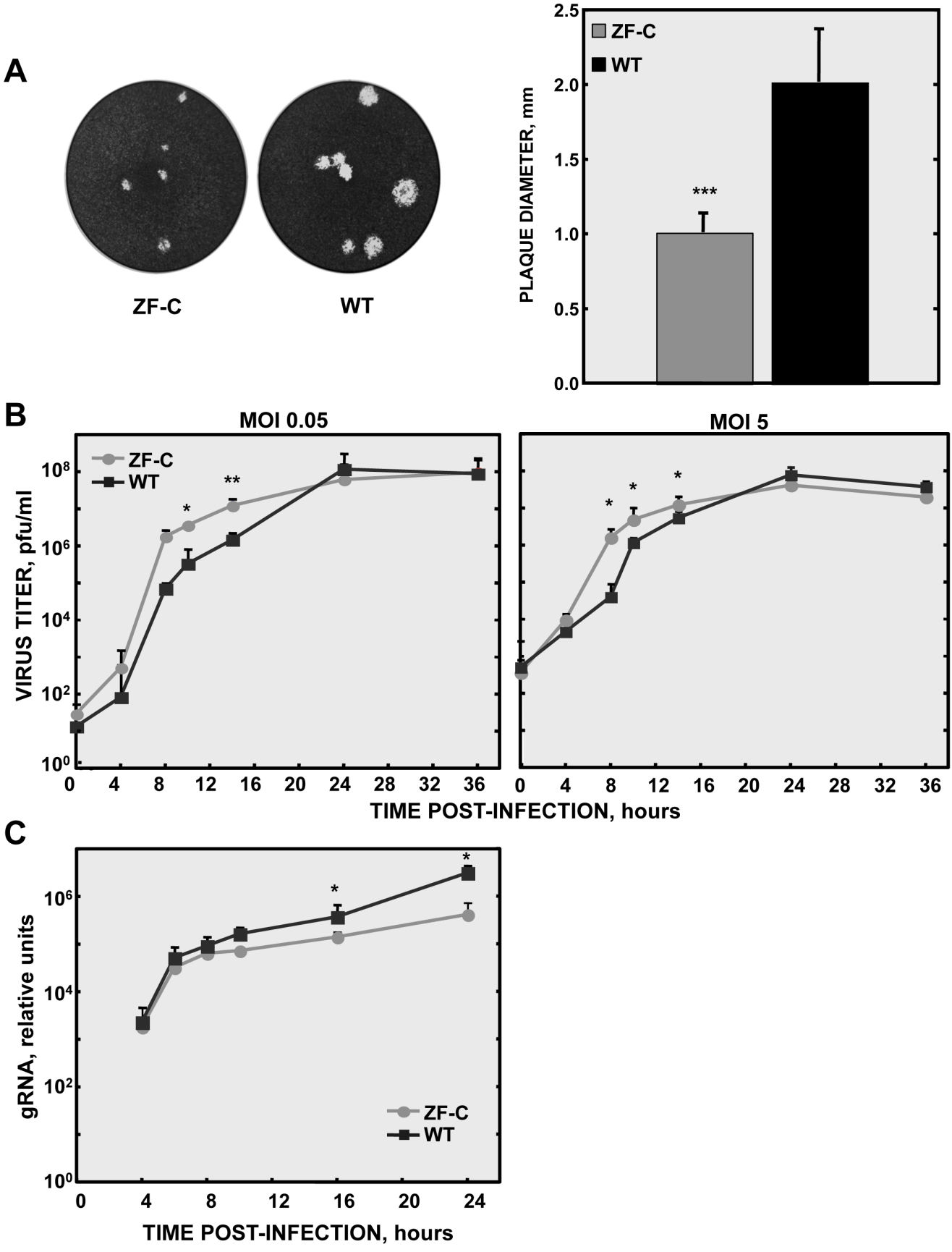

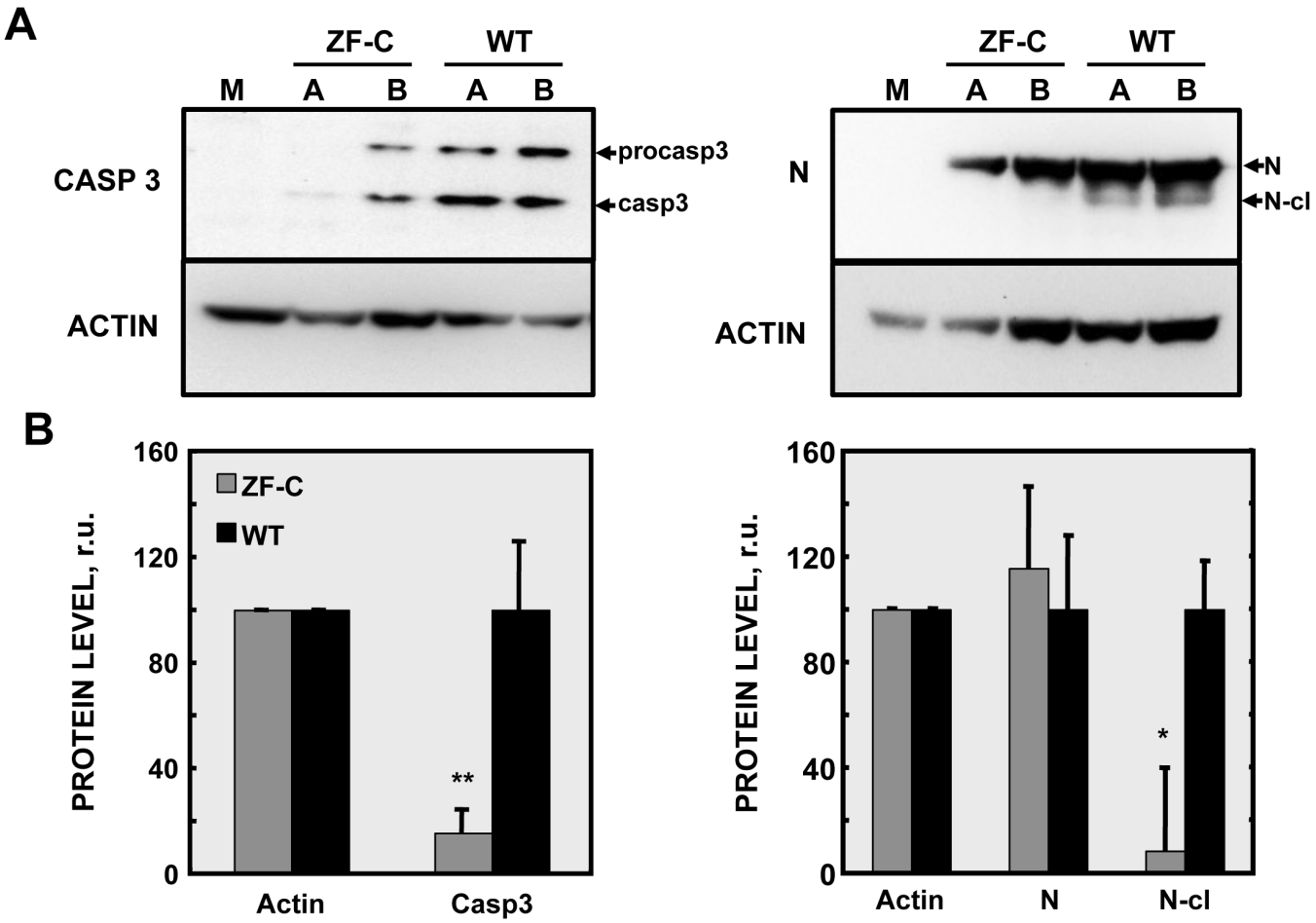

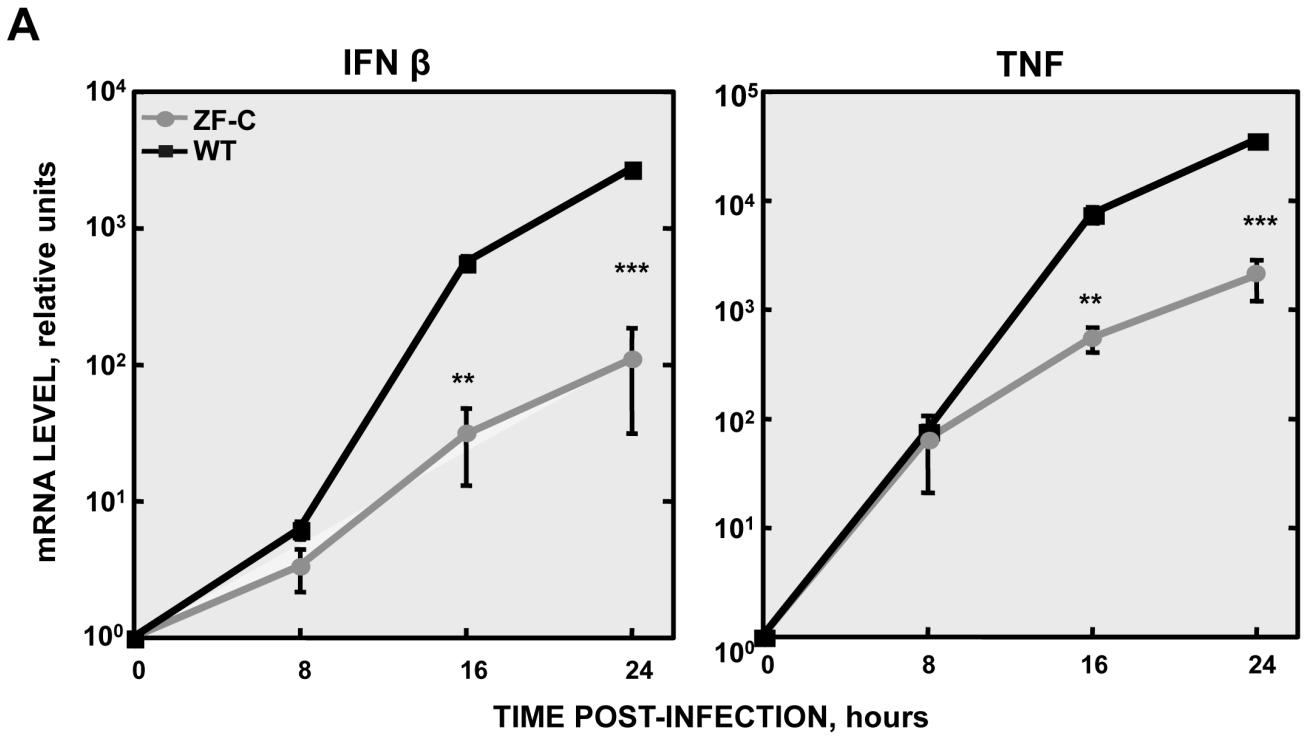

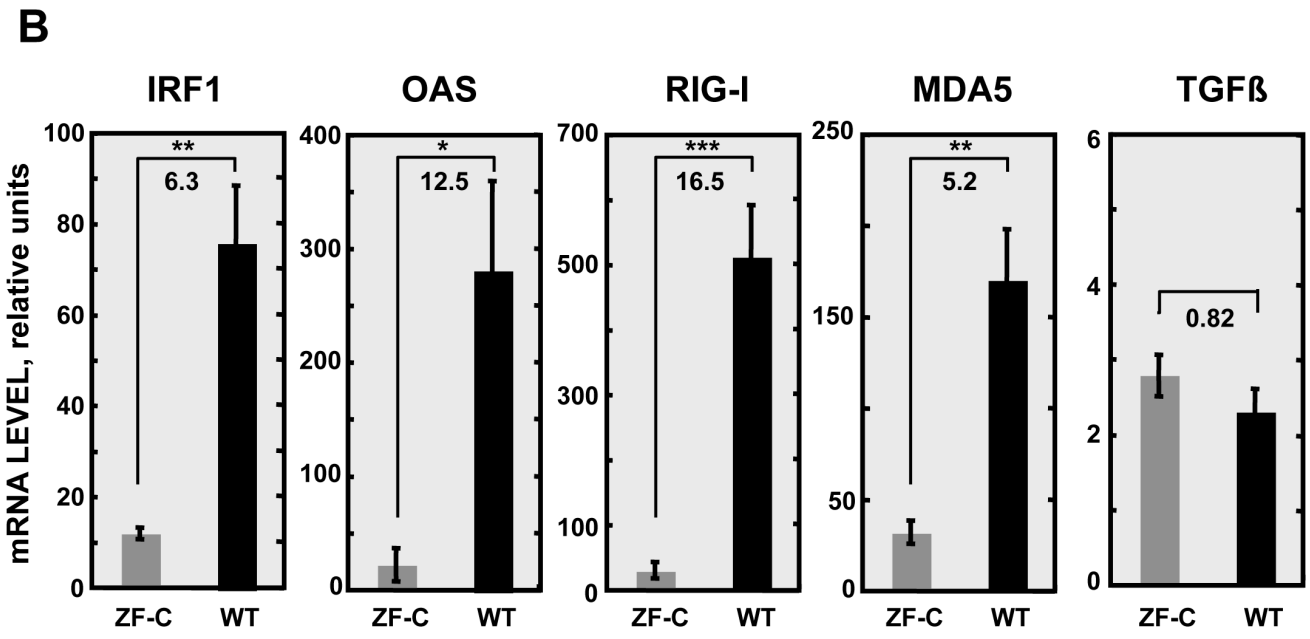

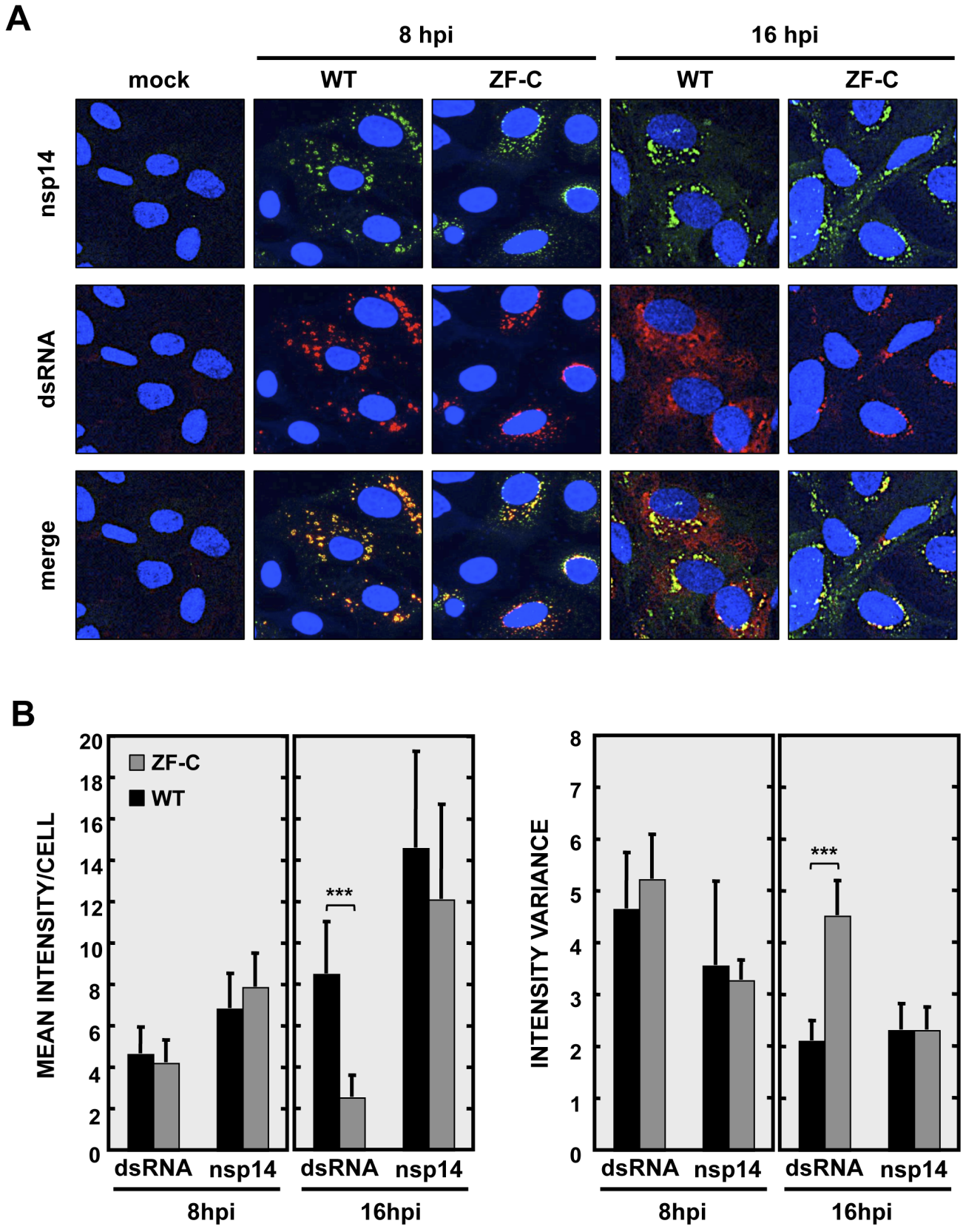

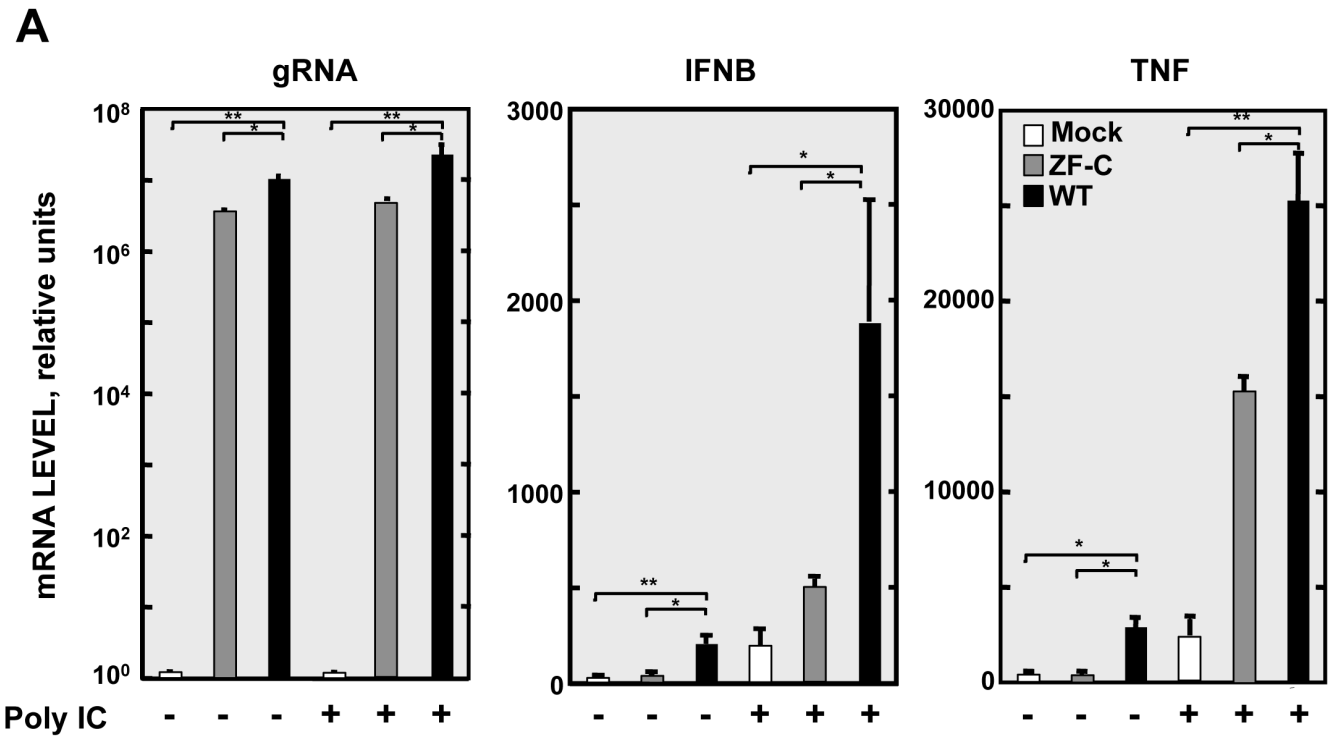

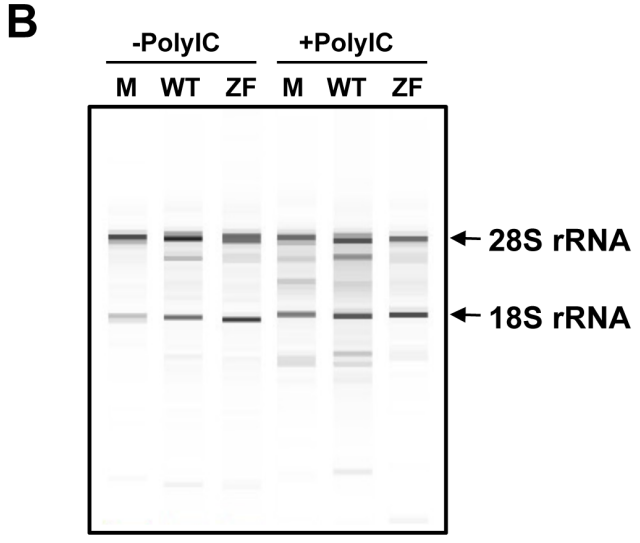

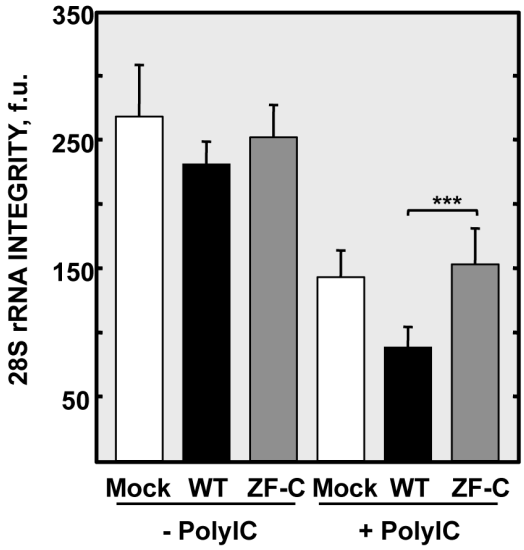

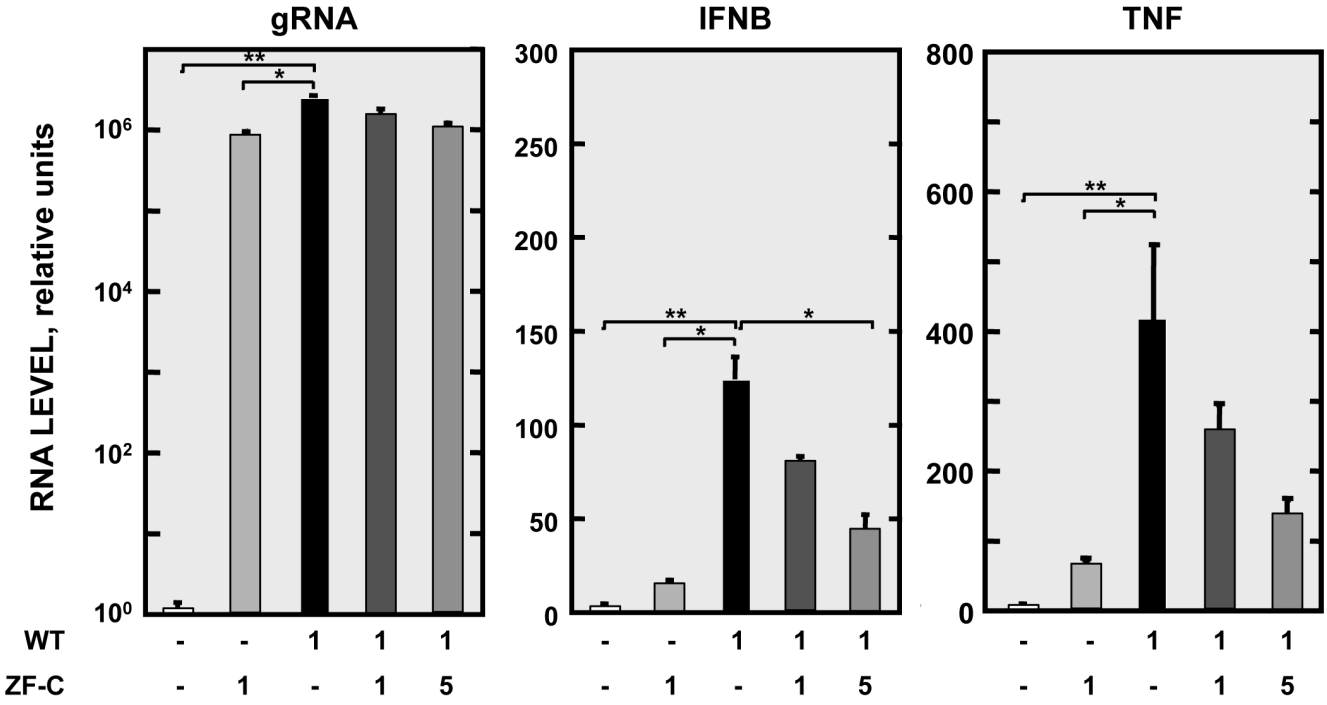

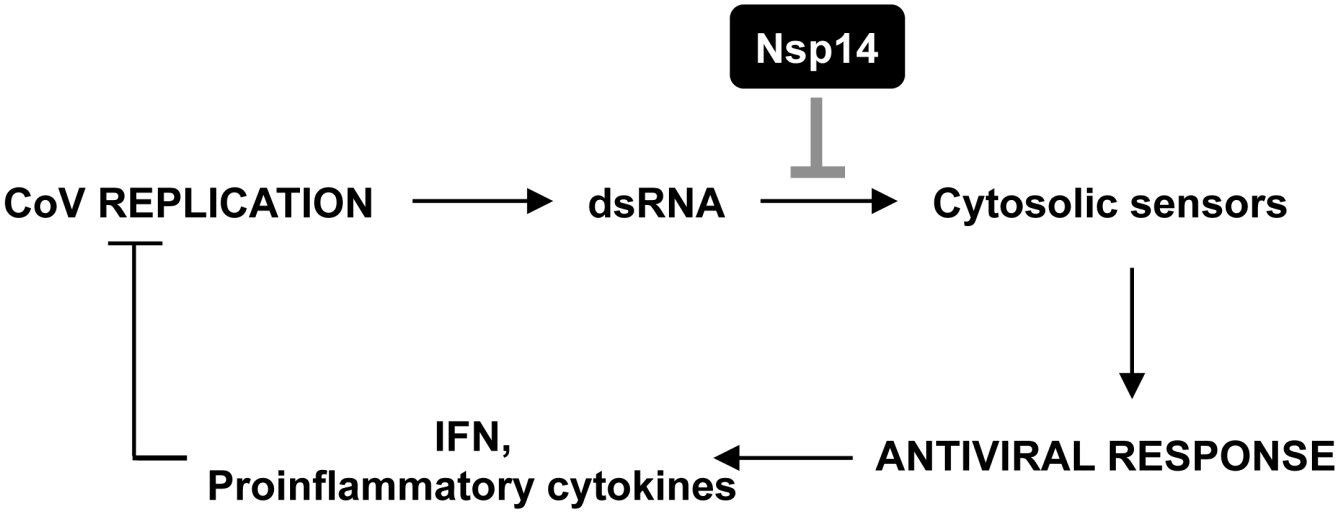

Table 1. Primers used for nsp14 mutagenesis

MUTANT	PRIMER[a]	SEQUENCE (5'-3') [b]
nsp14-ExoI	ExoI_VS	CTTGGGTTTG**CA**GTTG**CT**GGTGCACATG
	ExoI_RS	CATGTGCACC**AG**CAAC**TG**CAAACCCAAG
nsp14-ExoIII	ExoIII_VS	GCTAGTGGTG**CG**GCTATCATGACTAG
	ExoIII_RS	CTAGTCATGATAGC**CG**CACCACTAGC
nsp14-ZF-H	CHCH_VS	CAAAAATGTGAA**CA**CGGCAAAAG
	CHCH_RS	CTTTTGCCG**TG**TTCACATTTTTG
nsp14-ZF-C	CCCC_VS	GCTTGCTTCAAG**TG**TGCATTAGGATG
	CCCC_RS	CATCCTAATGCA**CA**CTTGAAGCAAGC
nsp14-N7MTase	N7MTase_VS	GCTTGCTTCAAG**TG**TGCATTAGGATG
	N7MTase_RS	GATTACCCAC**CG**CGTGAATTGCAGC

[a] VS, forward primer; RS, reverse primer.
[b] Mutant nucleotides are in bold.

Table 2. TaqMan assays used for RT-qPCR of viral gRNA and sgmRNA

AMPLICON	TAQMAN ASSAY [a]		SEQUENCE (5'-3') [(b)]
	PrimerVS	RepVS	TTCTTTTGACAAAACATACGGTGAA
gRNA(+)	PrimerRS	RepRS	CTAGGCAACTGGTTTGTAACATCTTT
	Probe	Rep-MGB	FAM-AGGGCACCGTTGTCA-MGB
	PrimerVS	RepRS	CTAGGCAACTGGTTTGTAACATCTTT
gRNA(-)	PrimerRS	RepVS	CTAGGCAACTGGTTTGTAACATCTTT
	Probe	cRep-MGB	FAM-CTGTTCACCGTATGTTT-MGB
	PrimerVS	Ldrt-VS	CGTGGCTATATCTCTTCTTTTACTTTAACTAG
mRNA7(+)	PrimerRS	7 (38)-RS	AAAACTGTAATAAATACAGCATGGAGGAA
	Probe	mRNA7-MGB	FAM-CGAACTAAACGAGATGCT-MGB
	PrimerVS	7 (38)-RS	AAAACTGTAATAAATACAGCATGGAGGAA
mRNA(-)	PrimerRS	Ldrt-VS	CGTGGCTATATCTCTTCTTTTACTTTAACTAG
	Probe	cmRNA7-MGB	FAM-AGCATCTCGTTTAGTTCGAGT-MGB

[a] VS, forward primer; RS, reverse primer; MGB, minor groove binder group.
[b] FAM, 6-carboxyfluorescein.